Persistent scatterer interferometric synthetic aperture radar for crustal deformation analysis, with application to Volcán Alcedo, Galápagos

A. Hooper,[1,2] P. Segall,[1] and H. Zebker[1]

[1]   While conventional interferometric synthetic aperture radar (InSAR) is a very effective technique for measuring crustal deformation, almost any interferogram includes large areas where the signals decorrelate and no measurement is possible. Persistent scatterer (PS) InSAR overcomes the decorrelation problem by identifying resolution elements whose echo is dominated by a single scatterer in a series of interferograms. Existing PS methods have been very successful in analysis of urban areas, where stable angular structures produce efficient reflectors that dominate background scattering. However, man-made structures are absent from most of the Earth's surface. Furthermore, existing methods identify PS pixels based on the similarity of their phase history to an assumed model for how deformation varies with time, whereas characterizing the temporal pattern of deformation is commonly one of the aims of any deformation study. We describe here a method for PS analysis, StaMPS, that uses spatial correlation of interferogram phase to find pixels with low-phase variance in all terrains, with or without buildings. Prior knowledge of temporal variations in the deformation rate is not required for their identification. We apply StaMPS to Volcán Alcedo, where conventional InSAR fails because of dense vegetation on the upper volcano flanks that causes most pixels to decorrelate with time. We detect two sources of deformation. The first we model as a contracting pipe-like body, which we interpret to be a crystallizing magma chamber. The second is downward and lateral motion on the inner slopes of the caldera, which we interpret as landsliding.

1.   Introduction

[2]   Volcán Alcedo is one of six volcanoes located on Isla Isabela in the Galápagos Archipelago (Figure 1). Alcedo is unusual in that it is the only active Galápagos volcano known to have erupted rhyolite as well as basalt [*Geist et al.*, 1994]. The last known eruption occurred in late 1993 from the south caldera wall [*Green*, 1994]. Deformation of the caldera was detected by *Amelung et al.* [2000], who carried out interferometric analysis of synthetic aperture radar (SAR) data acquired over Alcedo between 1992 and 1999. However, they found the correlation to be too low to determine the deformation signal on the volcano flanks and were therefore unable to draw any conclusions about the source of the deformation. No measurements of surface displacement have been made on Alcedo by any other means, and displacements inferred from SAR data are therefore all

we can currently use to constrain the movement of subsurface magma and volatiles. Conventional interferometric SAR (InSAR) fails on the upper flanks of Alcedo because a significant amount of vegetation is present and this leads to temporal decorrelation for most pixels in the image.

[3]   When a SAR image is formed, even at the highest possible resolution, the value for each pixel remains the coherent sum of the returns from many scatterers on the ground. If these scatterers move with respect to each other between satellite passes, as is expected to be the case when many scatterers are vegetation, the phase of the return will vary in a random manner which leads to decorrelation. If, however, a pixel is dominated by one stable scatterer that is brighter than the background scatterers, the variance in the phase of the echo due to relative movement of the background scatterers will be reduced, and may be small enough to enable extraction of the underlying deformation signal (Figure 2). *Hooper et al.* [2004] identified this type of pixel as a persistent scatterer (PS) pixel. Physically, these stable scatterers might be a tree trunk or a single large rock or facet amongst the vegetation.

[4]   Methods to identify and isolate these PS pixels in interferograms have been developed by several groups [e.g., *Ferretti et al.*, 2001; *Crosetto et al.*, 2003; *Lyons and*

[1]Department of Geophysics, Stanford University, Stanford, California, USA.
[2]Now at Nordic Volcanological Center, University of Iceland, Reykjavik, Iceland.
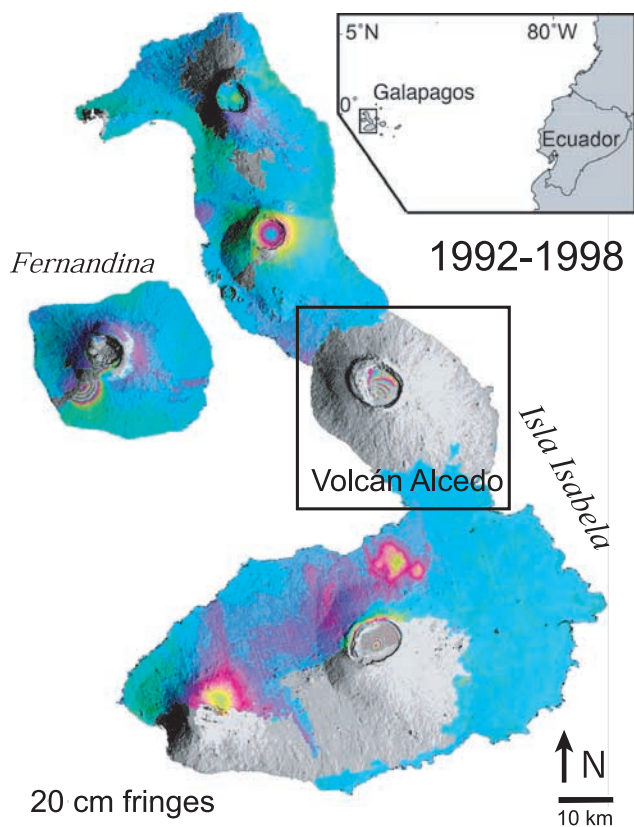
Figure 1. Location of Volcán Alcedo on Isla Isabela, Galápagos. The image is adapted from *Amelung et al.* [2000](by permission from Macmillan Publishers Ltd., *Nature*, copyright 2000) and shows line-of-sight ground displacements between 1992 and either 1997 or 1998, depending on the volcano.

Sandwell, 2003; *Werner et al.*, 2003; *Kampes*, 2005]. All of these methods use a functional model of how deformation varies with time to identify PS pixels, and have been very successful in identifying PS pixels in urban areas undergoing primarily steady state or periodic deformation. In these algorithms an initial set of PS pixels with a high signal-to-noise ratio (SNR) is identified by analyzing the amplitude variation, pixel by pixel, in a series of interferograms. Approaches include analysis of each pixel alone [e.g., *Ferretti et al.*, 2001] and comparison with surrounding pixels [e.g., *Adam et al.*, 2005]. Once an initial set of amplitude-stable pixels has been identified, each candidate pixel is tested for phase stability by examining its phase differences with nearby candidates. Only a pixel whose phase history is similar to the assumed model of deformation is deemed stable and not merely the result of random chance. In this manner a network of reference PS pixels is identified that is then used to find additional PS pixels by further phase analysis of all (or a subset of) the remaining pixels.

[5] This approach can fail for two reasons, both related to the fact that the data are "wrapped" or modulo 2π. For reliable "unwrapping" or estimation of integer ambiguities, unmodeled phase must be small; *Colesanti et al.* [2003b] estimate that it must be less than 0.6 rad.

[6] First, it can fail if the distance between neighboring PS pixels is too large, such that the contribution to the unmodeled phase from the difference in delay along the raypaths through the atmosphere exceeds the limit for reliable unwrapping. For common atmospheric conditions, the PS pixel density should exceed 3 to 4 per km^2 [*Colesanti et al.*, 2003b]. The initial selection using amplitude variation finds most bright PS pixels, such as those from man-made structures, and therefore works well in urban areas where the density of structures is high. However, in most natural terrains, including the majority of volcanoes, bright scatterers are rare and the density of reference PS pixels is generally too low to form a closely spaced reference network. This is the case for Long Valley volcanic caldera [*Hooper et al.*, 2004] and the central San Andreas Fault zone [*Johanson and Bürgmann*, 2001].

[7] The second limitation is that an approximate model for the temporal variation in deformation is needed to isolate the deformation signal from atmospheric, topographic and other phase errors. As the time dependence of deformation is not usually known a priori, it is usually assumed to be approximately constant in rate, or periodic in nature. If PS pixels can be identified, deviations from the initial parametric model may be estimated from the phase residuals [*Ferretti et al.*, 2000; *Colesanti et al.*, 2003b; *Kampes*, 2005]. Pixels can only be identified, however, when the deviations from the model are sufficiently small that unwrapping is reliable, as in the San Francisco Bay Area [*Ferretti et al.*, 2004; *Hilley et al.*, 2004], where deformation is due primarily to steady strain accumulation on various fault systems. In cases where deformation varies too much from steady state, such as many volcanoes and landslides, as well as certain tectonic settings e.g., those dominated by postseismic deformation, a reliable network of reference PS pixels will not result. A method is required that produces a time series of deformation, with no prior assumptions about its temporal nature.

[8] *Hooper et al.* [2004] introduced a PS method to extract the deformation signal from SAR data acquired over Long Valley caldera, an area that contains few man-made
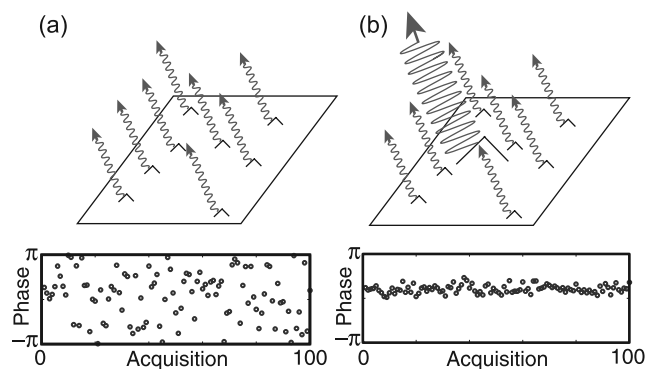

Figure 2. Phase simulations for (a) a distributed scatterer pixel and (b) a persistent scatterer pixel. (top) Cartoons representing the scatterers contributing to the phase of one pixel in an image and (bottom) simulations of the phase for 100 iterations, with the smaller scatterers moving randomly between each iteration. The brighter scatterer in Figure 2b is 3 times brighter than the sum of the smaller scatterers.
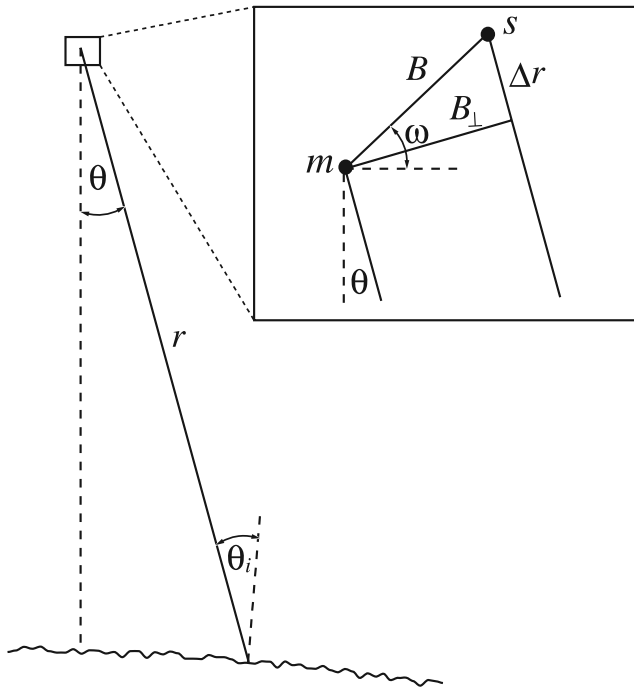
Figure 3. Imaging geometry for satellite radar interferometry. The sensor is moving into the plane of the paper, its position at the time of the master acquisition marked by m and at the time of the slave acquisition by s. B is the baseline distance between the sensor positions at the two times, with $B_\perp$ being the perpendicular component of B, r is the range from the sensor to the Earth's surface, ω is the angle between the baseline vector and the horizontal, θ is the look angle and θ_i is the angle of incidence at the Earth's surface.

structures and that deformed at variable rates during the time interval analyzed. *Hole et al.* [2006] also applied a variation of this method to the Taupo volcanic zone, New Zealand. In this paper, we report on significant improvements to the method which increase the accuracy of the estimated displacements and also make it applicable in areas with widely varying deformation gradients. We first describe in detail our method, StaMPS (Stanford Method for PS), for identifying PS pixels and estimating their displacements. We then apply StaMPS to SAR data acquired over Volcán Alcedo and model the source of the deformation seen in the resulting PS interferograms.

[9] There are four parts to StaMPS, each discussed in detail in sections 2–5:

[10] 1. For interferogram formation (section 2), there are aspects of interferogram formation for PS processing that differ to conventional interferogram formation. We summarize all the steps involved and describe the differences in detail. We also discuss the error terms associated with the processing.

[11] 2. For phase stability estimation (section 3), we make an initial selection of candidate pixels based on analysis of amplitude and then use phase analysis to estimate the phase stability of these pixels in an iterative process. Finally, there is an optional step to estimate the phase stability of those pixels that were initially rejected based on their amplitude characteristics.

[12] 3. For PS selection (section 4), we estimate for each pixel the probability it is a PS pixel based on a combination of amplitude and estimated phase stability. We then use the estimated probabilities to select PS pixels, rejecting those that appear to be persistent only in certain interferograms and those that appear to be dominated by scatterers in adjacent PS pixels.

[13] 4. For displacement estimation (section 5), once selected, we isolate the signal due to deformation in the PS pixels. This involves unwrapping the phase values and subtracting estimates of various nuisance terms.

2. Interferogram Formation

[14] For PS systems relying on a functional temporal model to select PS pixels, typically at least 25 interferograms are required to obtain reliable results [*Colesanti et al.*, 2003a]. Using StaMPS, however, fewer interferograms are required. We find that 12 interferograms are usually sufficient to identify a network of PS pixels and, in one case at least, have even been able to identify PS pixels using just four interferograms. The limiting factor is the accuracy in estimation of the look angle error (equation (18)), which is aided by good digital elevation model (DEM) accuracy and high SNR. The accuracy of the estimated look angle error and hence the estimated deformation signal improves as the number of interferograms increases, so it is desirable to use as many images as possible.

[15] It is possible to carry out PS analysis jointly on data acquired by sensors with different carrier frequencies, for example, data acquired by the ERS and ENVISAT satellites [e.g., *Adam et al.*, 2005; *Arnaud et al.*, 2004; *Arrigoni et al.*, 2004]. However, the number of PS pixels is reduced as only pixels dominated by the most point-like scatterers remain correlated at different frequencies. Because PS pixels in nonurban terrains tend to be less point-like in their scattering characteristics, we only consider here interferometry between images acquired by sensors with the same carrier frequency to maximize the number of PS pixels identified.

[16] There are several aspects of interferogram formation for StaMPS that differ from conventional InSAR processing, which we describe below, together with a discussion of the error terms that arise in interferometric processing.

2.1. Decorrelation and Choice of Master Image

[17] Suppose we form N single-look interferograms from $N + 1$ images acquired at different times, all with respect to one master image. We choose as the master, the image that minimizes the sum decorrelation, i.e., maximizes the sum correlation, of all the interferograms. The correlation is a product of four terms, dependent on time interval (T), perpendicular baseline ($B_\perp$, see Figure 3) difference in Doppler centroid (F_{DC}) and thermal noise [*Zebker and Villasenor*, 1992]. A simple model for the total correlation, ρ_{total}, is

$$\rho_{\text{total}} = \rho_{\text{temporal}}\rho_{\text{spatial}}\rho_{\text{doppler}}\rho_{\text{thermal}}$$

$$\approx \left[1 - f\left(\frac{T}{T^c}\right)\right]\left[1 - f\left(\frac{B_\perp}{B_\perp^c}\right)\right]\left[1 - f\left(\frac{F_{DC}}{F_{DC}^c}\right)\right]\rho_{\text{thermal}}, \quad (1)$$

where

$$f(x) = \begin{cases} x, \text{for } x \leq 1 \\ 1, \text{for } x > 1 \end{cases},$$

ρ denotes correlation and superscript c denotes the critical parameter values, i.e., the value beyond which an interferogram exhibits almost complete decorrelation. The critical values are dependent on the data set, but typical values for data acquired by the ERS satellites in arid regions are $T^c = 5$ years, $B_\perp^c = 1100$ m and $F_{DC}^c = 1380$ Hz. We choose the master that maximizes $\Sigma_{i=1}^{N}\rho_{\text{total}}$, assuming a constant value for ρ_{thermal}.

[18] We do not apply any spectral filtering in range or azimuth, which would increase the correlation, as this would coarsen the resolution. Generally, the finer the resolution, the fewer scatterers will be contained within each resolution cell, and the greater the chance of the cell being dominated by one scatterer. The trade-off is that except for truly point-like PS pixels, phase values will include decorrelation noise related to perpendicular baseline and Doppler separation.

[19] Our algorithm for PS identification does not actually require that all interferograms are formed with respect to one master, only that all are coregistered to one master. Although we have not implemented this option in our code, combinations of interferograms using multiple masters may be chosen to increase the sum correlation.

2.2. Coregistration

[20] Some interferograms have values of temporal separation, perpendicular baseline and Doppler separation that are larger than usual for conventional InSAR. This fact leads to high decorrelation and a corresponding low coherence which make standard coregistration routines, based on cross correlation of amplitude, fail. To avoid this problem, we have developed a coregistration algorithm that uses an amplitude based algorithm to estimate offsets in position between pairs of images with good correlation. The function that maps the master image to each other image is then estimated by weighted least squares inversion (Appendix A).

[21] Once the mapping functions are estimated, we resample each image to the master coordinate system, using a 12 point raised cosine interpolation kernel. Then we form a raw interferogram by differencing the phase of each image to the phase of the master.

2.3. Geometric Phase Correction

[22] Raw interferograms contain a geometric phase term which is due to the master and slave images being acquired from different points in space. As in conventional InSAR, we correct for this geometric phase in two steps. First, we flatten the interferograms, which involves correcting the phase of each pixel as if the scattering surface were lying on a reference ellipsoid. Next, we estimate the phase due to the deviation of the real surface from the reference ellipsoid by transforming a DEM into the radar coordinate system. Two error terms arise in this processing, look angle error and squint angle error. For pixels with many distributed scatterers, which is the usual situation for conventional interferometry, the look angle error is due almost entirely to

error in the DEM, and is commonly referred to as DEM error. For PS pixels, however, there is also a contribution due to the difference in range between the position of the dominant scatterer and the center of the ground patch that is resolved by the pixel; hence we prefer the more general term. Squint angle error is commonly avoided in conventional InSAR by processing both images to a common squint angle. However, this coarsens azimuthal resolution, which, as discussed in section 2.1, we wish to make as fine as possible to identify PS pixels.

2.3.1. Look Angle Error

[23] The geometric phase due to the change in look angle, ϕ_θ, is proportional to the change in range, Δr, between the master and slave geometry,

$$\phi_\theta = -\frac{4\pi}{\lambda}\Delta r, \tag{2}$$

where λ is the radar wavelength. The minus sign comes from the definition of the phase measured at the sensor being phase delay. From the geometry (Figure 3),

$$(r + \Delta r)^2 = r^2 + B^2 - 2rB\cos\left(\frac{\pi}{2} - \theta + \omega\right)$$
$$= r^2 + B^2 - 2rB\sin(\theta - \omega), \tag{3}$$

where r is the range in the master geometry, B is the baseline distance between the slave and master sensor position, θ is the look angle in the master geometry and ω is the angle between the baseline vector and the horizontal. Differentiating and using equation (2) gives

$$\frac{\partial\phi_\theta}{\partial\theta} = \frac{4\pi}{\lambda}\frac{B\cos(\theta - \omega)r}{(r + \Delta r)}. \tag{4}$$

[24] Typically $\Delta r \ll r$ so this simplifies to

$$\frac{\partial\phi_\theta}{\partial\theta} \approx \frac{4\pi}{\lambda}B\cos(\theta - \omega). \tag{5}$$

[25] Neglecting any error in $B\cos(\theta - \omega)$, which is included in an orbit error term (equation (10)), we find then that the error, $\Delta\phi_\theta$, in our estimate of $\widehat{\phi_\theta}$ depends only on $\Delta\theta$, the error in our knowledge of θ and for small $\Delta\theta$

$$\Delta\phi_\theta \approx \frac{4\pi}{\lambda}B\cos(\theta - \omega)\Delta\theta = \frac{4\pi}{\lambda}B_\perp(\theta)\Delta\theta, \tag{6}$$

where $B_\perp(\theta)$ is the perpendicular component of the baseline. From the geometry, $\Delta\theta$ is obviously dependent on the accuracy of the estimated height above the reference surface (Figure 3) but is also dependent on any difference in the position of the pixel phase center to that assumed in the flattening step. Specifically,

$$\Delta\theta = \frac{\Delta h\sin(\theta_i) + \xi\,\cos(\theta_i)}{r}, \tag{7}$$

where Δh is the error in height, ξ is the horizontal distance of the phase center from the middle of the pixel in range direction, and θ_i is the incidence angle. Thus, even if the

DEM were 100% accurate, there could still be an error in θ due to both the lateral offset of the phase center itself and any variation in height due to this offset. In the case that we consider here, where carrier frequency does not vary between passes, the DEM error is indistinguishable from the error due to phase center uncertainty. With varying carrier frequency, separation of the two errors would be possible [Colesanti et al., 2003b; Kampes, 2005], yielding more accurate positioning of the scatterer; however, the above mentioned limitation of using varying carrier frequencies, that only the most point-like pixels remain persistent, would apply. In any case, the positional accuracy of several meters that is already obtained is sufficient for most deformation studies.

[26] As the look angle error term is estimated later in the PS processing, the accuracy of the DEM is not usually important, although higher accuracy reduces the ambiguity in the estimation step, and thus is important in the case where only a few (<12) interferograms are available.

2.3.2. Squint Angle Error

[27] There is a similar error term due to the difference in squint angle between passes. SAR azimuth focusing assumes that the phase center of the pixel is in the center. The additional phase introduced if the phase center deviates from the pixel center in azimuth direction, by an amount η, cancels when the squint angle is the same for both the master and slave acquisition. When the squint angles differ, an error term

$$\Delta\phi_\vartheta = \frac{2\pi}{v} F_{DC} \eta \qquad (8)$$

arises, where v is the sensor velocity (see Kampes [2005] for a derivation). In the data sets we have analyzed until now, F_{DC} is generally small and $\Delta\phi_\vartheta$ is expected to be less than 0.2 rad. Furthermore, F_{DC} is somewhat correlated with time. As deformation is also correlated with time, there is the potential for the phase due to deformation, which is often much larger, leaking into any estimate for $\Delta\phi_\vartheta$. We therefore do not attempt to estimate this term and, instead, treat it as noise.

2.4. Geocoding

[28] Finally, we estimate the position of every pixel in a geocoded reference frame using the orbital parameters and the DEM. Theoretically, our estimates of position could be improved using various parameters estimated during processing, but for the purposes of most deformation modeling, positional accuracy to within several meters is usually sufficient.

3. Phase Stability Estimation

[29] Initially, we select a subset of pixels based on analysis of their amplitudes, rejecting those least likely to be PS pixels. We then estimate the phase stability of each of these pixels through phase analysis, which we successively refine in a series of iterations. Finally, we include an optional step to estimate the phase stability of those pixels that were not included in the initial amplitude-based selection.

3.1. Amplitude Analysis

[30] Although it is the phase stability of a pixel that defines a PS pixel, there is a statistical relationship between amplitude stability and phase stability, that makes consid-

eration of amplitude useful for reducing the initial number of pixels for phase analysis. Later, we also include amplitude characteristics in estimating the probability of a pixel being a PS pixel, as discussed in section 4.

[31] The amplitude dispersion index, D_A, is defined by Ferretti et al. [2001] as

$$D_A \equiv \frac{\sigma_A}{\mu_A}, \qquad (9)$$

where σ_A and μ_A are the standard deviation and the mean of a series of amplitude values, respectively. Ferretti et al. [2001] threshold on D_A to select a subset of pixels where most are PS pixels. We use D_A differently, to select a subset of pixels that includes almost all of the PS pixels in the data set. The threshold value we use is consequently higher, typically in the region of 0.4, which leads to most of the selected pixels not being PS pixels (see Appendix B). There is an optional later step, described in section 3.3, in which pixels above this threshold are also analyzed for phase stability.

3.2. Phase Analysis

[32] Having selected a subset of pixels as initial PS candidates, we estimate the phase stability for each of them using phase analysis. The wrapped phase, $\psi_{x,i}$, of the xth pixel in the ith "flattened" and topographically corrected interferogram can be written as the wrapped sum of 5 terms,

$$\psi_{x,i} = W\{\phi_{D,x,i} + \phi_{A,x,i} + \Delta\phi_{S,x,i} + \Delta\phi_{\theta,x,i} + \phi_{N,x,i}\}, \qquad (10)$$

where $\phi_{D,x,i}$ is the phase change due to movement of the pixel in the satellite line-of-sight (LOS) direction, $\Delta\phi_{\theta,x,i}$ is the residual phase due to look angle error, $\phi_{A,x,i}$ is the phase due to the difference in atmospheric delay between passes, $\Delta\phi_{S,x,i}$ is the residual phase due to satellite orbit inaccuracies, $\phi_{N,x,i}$ is a noise term due to variability in scattering, thermal noise, coregistration errors and uncertainty in the position of the phase center in azimuth, and $W\{\cdot\}$ is the wrapping operator. The pixels we seek as PS are those where $|\phi_{N,x,i}|$ is small enough that it does not completely obscure the signal. As the phase is wrapped, this term must certainly be less than π, but in order to correctly estimate the integer ambiguity in the number of wraps when estimating the spatially uncorrelated look angle error, $\Delta\theta_x^u$ in equation (18), it must be even smaller in practice.

[33] Variation in the first four terms of equation (10) dominates the noise term, making it difficult to identify which scatterers are persistent directly from the wrapped phase. Hence we estimate these four terms and subtract them, giving an estimate for $\widehat{\phi}_{n,x,i}$ which we assess statistically. We then reestimate the first four terms, using the statistics of $\widehat{\phi}_{n,x,i}$ to weight the contribution of each pixel to the reestimaton, and subtract the reestimated values from equation (10) to give a new estimate of $\widehat{\phi}_{n,x,i}$. We iterate around this loop, refining our estimates of $\widehat{\phi}_{n,x,i}$ each time, until the values converge, which generally occurs after only a few iterations.

[34] The deformation signal we are interested in is that due to deformation of the Earth's surface, which is correlated spatially. There could also be signal associated with the isolated movement of individual bright scatterers, but
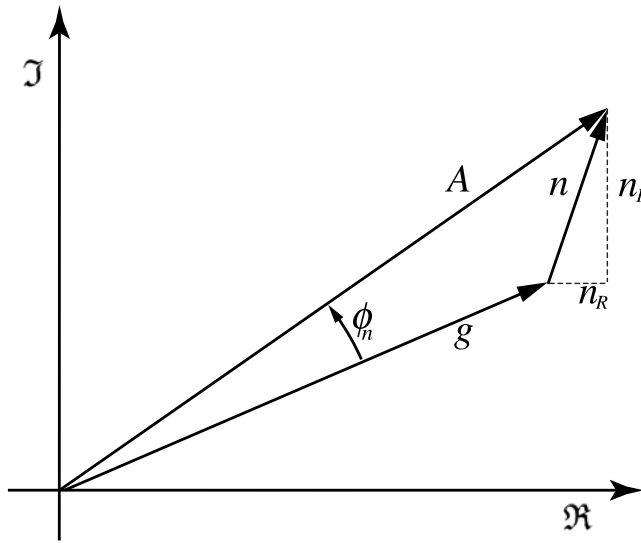
that real and imaginary components of the noise, $n_{R,x,i}$ and $n_{I,x,i}$, respectively, are characterized by a single Gaussian distribution with zero mean and standard deviation $\sigma_{n,x}$, then SNR $= g_x^2/2\sigma_{n,x}^2$. Our estimate of $\widehat{g}_x$ is then simply

$$\widehat{g}_x = \frac{1}{N}\sum_{i=1}^{N} A_{x,i}\cos\phi_{N,x,i}, \tag{11}$$

which follows from the fact that $g_{x,i} = A_{x,i}\cos\phi_{N,x,i} - n_{\parallel,x,i}$ where $n_{\parallel,x,i}$ is the signal parallel component of noise, the mean of which is zero. Our estimate for $\widehat{\sigma}_{n,x}^2$ is given by

$$\widehat{\sigma}_{n,x}^2 = \frac{\sum_{i=1}^{N}\left(n_{I,x,i}^2 + n_{R,x,i}^2\right)}{2N}$$
$$= \frac{\sum_{i=1}^{N}\left(A_{x,i}^2 sin^2\phi_{N,x,i} + \left(A_{x,i}\cos\phi_{N,x,i} - g_x\right)^2\right)}{2N}. \tag{12}$$

[36] Substituting for g_x with $\widehat{g}_x$ gives

$$\widehat{\sigma}_{n,x}^2 = \frac{1}{2}\left[\frac{\sum_{i=1}^{N} A_{x,i}^2}{N} - \left(\frac{\sum_{i=1}^{N} A_{x,i}\cos\phi_{N,x,i}}{N}\right)^2\right]. \tag{13}$$

[37] We also experimented with other weight selection methods, for example, weighting each pixel based on the probability that it is persistent. Empirically, we find that setting the amplitude to $1/[P(x \in PS)]^2$, where $P(x \in PS)$ is the probability that the pixel is a PS pixel (see Appendix C), can give better results than weighting with the SNR, in the sense that more PS pixels are found.

[38] To enable use of the two-dimensional fast Fourier transform (2-D FFT), the complex phase of the weighted PS pixels is sampled to a grid with spacing over which little variation in phase is expected (typically 40 to 100 m). Where multiple pixels fall in the same grid cell, their complex values are summed. We apply the 2-D FFT to a grid size of typically 32×32 or 64×64 cells, depending on over what distance we expect pixels to remain spatially correlated. The adaptive part of the filter determines the passband based on the dominant frequencies present in the phase of the pixels themselves. The response is calculated as

$$H(u,v) = |Z(u,v)|, \tag{14}$$

where $Z(u,v)$ is the smoothed intensity of the 2-D FFT [Goldstein and Werner, 1998]. We smooth the intensity by convolution with a 7×7 pixel Gaussian window. We combine the adaptive phase filter response, $H(u,v)$, with a narrow low-pass filter response, $L(x,y)$, to form the new filter response,

$$G(u,v) = L(u,v) + \beta\left(\frac{H(u,v)}{\overline{H}(u,v)} - 1\right)^{\alpha}, \tag{15}$$

where $L(u,v)$ is a fifth-order Butterworth filter, with a typical cutoff wavelength of 800 m, α and β are adjustable weighting parameters, typical values being 1 and 0.3, respectively, and $\overline{H}(u,v)$ is the median value of $H(u,v)$.

Figure 4. Model for pixel amplitude, A. The signal is assumed to have constant amplitude, g. The real and imaginary components of the noise, n_R and n_I, are characterized by the same Gaussian distribution.

we are not interested here in these movements and they can be considered noise. Variation in atmospheric delay between passes is due mainly to variation in the total electron content (TEC) of the ionosphere and water vapor content of the troposphere. Both of these quantities are correlated spatially [Hanssen, 2001]. Orbital errors are also correlated spatially in azimuth, and interferometric processing leads to spatial correlation of the residual orbit error term also in range. Finally, DEM error tends to be partly spatially correlated and this maps into the look angle error. Hence estimating the spatially correlated part of $\psi_{x,i}$ provides an estimate for the first three terms plus part of the fourth term in equation (10). Hooper et al. [2004] achieved this by calculating the mean of surrounding pixels that were judged most likely to be PS pixels. The number of pixels included in the mean was reduced with each iteration as confidence in ruling out pixels as PS increased. This method is, in effect, a crude low-pass filter implemented in the spatial domain and relies on knowing the length scale of the spatial correlation. While this method worked fine in Long Valley, where the limiting factor on distance of spatial correlation is the atmospheric term, in areas with steeper deformation gradients the deformation term can become the limiting factor, altering the length scale of correlation. A better approach is to apply a band-pass-filtering method that adapts to any phase gradient present in the data.

[35] We implement the band-pass filter as an adaptive phase filter combined with a low-pass filter, applied in the frequency domain. Each pixel is first weighted by setting the amplitude in all interferograms to an estimate of the SNR for the pixel, which in the first iteration we estimate as $1/\widehat{D}_A$. In subsequent iterations we use the amplitude and our estimate of $\widehat{\phi}_{N,x,i}$ to estimate SNR. Figure 4 shows the relationship between signal, noise, amplitude and phase noise for a single pixel in a single image. If we assume that the amplitude of the signal, g_x, remains constant and
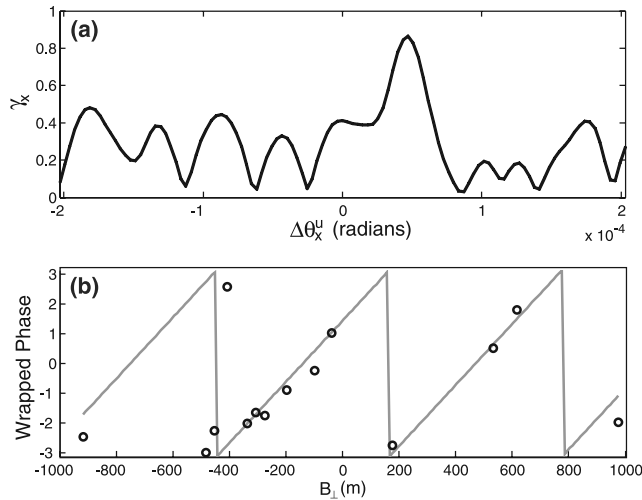
Figure 5. An example parameter space search for look angle error, $\Delta\theta_x^u$, for a PS pixel in the Alcedo descending orbit data set (see section 6). (a) Goodness of fit for trial values of $\Delta\theta_x^u$ and (b) a comparison between the data (circles) and phase values predicted by the value of $\Delta\theta_x^u$ with maximum γ_x (gray line).

[39] The resulting filtered phase value, $\widetilde{\psi}_{x,i}$, is a wrapped estimate of the spatially correlated parts of each of the terms on the right-hand side of equation (10), so subtracting $\widetilde{\psi}_{x,i}$ from $\psi_{x,i}$ and rewrapping gives

$$
\begin{aligned}
&W\left\{\psi_{x,i} - \widetilde{\psi}_{x,i}\right\} \\
&= W\left\{\phi_{D,x,i}^u + \phi_{A,x,i}^u + \Delta\phi_{S,x,i}^u + \Delta\phi_{\theta,x,i}^u + \phi_{N,x,i}^u\right\},
\end{aligned}
\tag{16}
$$

where ϕ^u denotes the spatially uncorrelated part of ϕ. We expect $\phi_{D,x,i}^u$, $\phi_{A,x,i}^u$ and $\Delta\phi_{S,x,i}^u$ to be small, as most of their power lies at longer wavelengths, so replacing their sum with $\delta_{x,i}$ in equation (16) gives

$$
W\left\{\psi_{x,i} - \widetilde{\psi}_{x,i}\right\} = W\left\{\Delta\phi_{\theta,x,i}^u + \phi_{N,x,i}^u + \delta_{x,i}\right\}.
\tag{17}
$$

[40] Equation (6) describes an approximate linear relationship between $\Delta\phi_{\theta},x,i$ and $\Delta\theta_x$. As long as $\Delta\phi_{\theta,x,i}^u$ contains approximately the same frequency components for all i, it follows that the same approximate relationship holds between $\Delta\phi_{\theta,x,i}^u$ and $\Delta\theta_x^u$. Substituting for $\Delta\phi_{\theta,x,i}^u$ in equation (17) gives

$$
\begin{aligned}
&W\left\{\psi_{x,i} - \widetilde{\psi}_{x,i}\right\} \\
&\approx W\left\{\frac{4\pi}{\lambda}B_{\perp,x,i}\Delta\theta_x^u + \phi_{N,x,i}^u + \delta_{x,i}\right\}.
\end{aligned}
\tag{18}
$$

[41] Because $B_{\perp,x,i}$ is not expected to correlate with $\phi_{N,x,i}^u$ or $\delta_{x,i}$, we can estimate $\Delta\widehat{\theta}_x^u$ in a least squares sense. The contribution from the master image to $\phi_{N,x,i}^u + \delta_{x,i}$ will be present in every interferogram, causing a constant offset, $\phi_x^{m,u}$, that we must also resolve in our least squares inversion. Since the phase is wrapped, the inversion is not linear. We implement the inversion as a rough search of

parameter space, followed by a linear inversion to estimate the best fitting model in the region of the rough estimate. We typically limit the rough search to values of $\Delta\widehat{\theta}^u$ equivalent to ±10 m of height error and in increments such that the range of $\Delta\phi_{\theta,x}^u$ increases by $\pi/4$ (Figure 5). The inversion could also be implemented using the least squares ambiguity decorrelation (LAMBDA) method, initially developed for fast GPS double-difference integer ambiguity estimation [*Teunissen*, 1995] and adapted for InSAR data by *Kampes* [2005]. However, we find that as implemented, the inversion is not a time-limiting step.

[42] From our estimate for $\Delta\widehat{\theta}_x^u$ we derive $\Delta\widehat{\phi}_{\theta,x,i}^u$ which we subtract from equation (17) to give

$$
W\left\{\psi_{x,i} - \widetilde{\psi}_{x,i} - \Delta\widehat{\phi}_{\theta,x,i}^u\right\} = W\left\{\phi_{N,x,i}^u + \delta'_{x,i}\right\},
\tag{19}
$$

where $\delta'_{x,i} = \delta_{x,i} + \Delta\phi_{\theta,x,i}^u - \Delta\widehat{\phi}_{\theta,x,i}^u$.

[43] We define a measure of the variation of this residual phase for a pixel as

$$
\gamma_x = \frac{1}{N}\left|\sum_{i=1}^{N}\exp\left\{\sqrt{-1}\left(\psi_{x,i} - \widetilde{\psi}_{x,i} - \Delta\widehat{\phi}_{\theta,x,i}^u\right)\right\}\right|,
\tag{20}
$$

where N is the number of interferograms. Assuming that $\phi_{N,x,i} \approx \phi_{n,x,i}^u$ and $\delta_{x,i} \approx 0$, γ_x is a measure of the phase noise level and an indicator of whether the pixel is a PS pixel. The measure γ_x is similar to a measure of coherence [*Bamler and Just*, 1993], although in time rather than in space as is generally implied by the term in reference to SAR interferograms. The measure differs from coherence in that amplitude is assumed to be constant at all times, as we wish to give every image equal weight. A pixel that is bright in one image and dark with random phase in all other images would have high coherence if amplitude were included whereas in reality it would not be a good PS pixel.

[44] The value of γ_x also depends on the accuracy of $\widetilde{\psi}_{x,i}$. In the case where all the phase values for the surrounding grid, to which the 2-D FFT is applied, are completely decorrelated, $\widetilde{\psi}_{x,i}$ will be random. The measure γ_x will then not be a true representation of the variation in residual phase for a pixel, and the pixel will likely not be selected.

3.3. Pixels With High-Amplitude Dispersion

[45] Some pixels with a high value of $\widehat{D}_A$, which are rejected by our initial thresholding (section 3.1), will have stable phase, although the proportion will be small (see Appendix B). Once the low-D_A pixels have been analyzed, we include an optional step to analyze the high-D_A pixels, using the filtered phase of the low-D_A pixels to calculate $\widetilde{\psi}_{x,i}$, and proceeding from equation (16) to calculate γ_x.

4. PS Selection

[46] Once we have converged on estimates for the phase stability of each pixel, we select those most likely to be PS pixels, with a threshold determined by the fraction of false positives we deem acceptable. We also seek to reject pixels that persist only in a subset of the interferograms and those that are dominated by scatterers in adjacent PS pixels.

[47] After every iteration we calculate the root-mean-square change in γ_x. When it ceases to decrease, the

solution has converged and the algorithm stops iterating. We then select pixels based on the probability they are PS pixels. Appendix C describes PS probability estimation based on γ_x alone. As there is a correlation between amplitude variance and phase stability (see section 3.1), we can calculate the probability more accurately still by considering the amplitude dispersion of the pixels, $\widehat{D}_{A,x}$, as well as γ_x. We bin the pixels by $\widehat{D}_{A,x}$, ensuring there are at least 10^4 pixels in every bin, and then bin by γ_x in increments of 0.01, resulting in the probability distribution, $p(\gamma_x, \widehat{D}_{A,x})$. For each bin in $\widehat{D}_{A,x}$, we estimate α, the proportion of the pixels that are PS pixels, as described in Appendix C. If only pixels with γ_x above a given threshold value, γ^{thresh}, are selected, the number of those pixels that are non-PS pixels is given by $(1 - \alpha) \int_{\gamma^{\text{thresh}}}^{1} p_B(\gamma_x) d\gamma_x$, where $p_B(\gamma_x)$ is the probability distribution for pixels with random phase. We find $\gamma^{\text{thresh}}(\widehat{D}_{A,x})$ for each bin in $\widehat{D}_{A,x}$ such that the fraction of pixels selected that are non-PS pixels (false positive identifications) is acceptable for our particular application, i.e.,

$$\frac{\left(1 - \alpha\left(\widehat{D}_{A,x}\right)\right) \int_{\gamma^{\text{thresh}}}^{1} p_B(\gamma_x) \, d\gamma_x}{\int_{\gamma^{\text{thresh}}}^{1} p\left(\gamma_x, \widehat{D}_{A,x}\right) d\gamma_x} = q, \quad (21)$$

where q is the specified acceptable fraction of false positives. As discussed in Appendix B, we generally expect γ_x, which is a measure of phase stability, to decrease with increasing $\widehat{D}_{A,x}$. This implies that as $\widehat{D}_{A,x}$ increases, $p(\gamma_x, \widehat{D}_{A,x})$ will skew to lower values of γ_x. The net effect on $\gamma^{\text{thresh}}(\widehat{D}_{A,x})$ is to increase with increasing $\widehat{D}_A$. Empirically we find that the relationship is approximately linear, i.e., $\gamma^{\text{thresh}} = \kappa \widehat{D}_A$ where κ is a constant. We find the best fitting κ by least squares inversion and select pixels for which $\gamma_x > \kappa \widehat{D}_{A,x}$ as our PS pixels.

4.1. Partially Persistent Scatterers

[48] The stability of a pixel may change during the time interval spanned by the data set, for example, if a dominant scatterer is added or removed. Another issue arises when the scattering characteristics of a dominant scatterer are altered, but the scatterer remains dominant. The pixel would then exhibit two intervals of phase stability, although one of the intervals would be decorrelated with respect to the master image. In both cases the pixel may still be identified if its mean variance is small enough, although in some images the phase will be dominated by noise. Furthermore, if the phase characteristics of whole areas of an image change between two passes, e.g., if a field is plowed or there is a new lava flow, the signal of all PS pixels selected in that area will be dominated by noise in some of the images.

[49] It would be possible to keep these pixels only for those images where they provide useful deformation signal, and reject them for all other images. However, the three-dimensional phase unwrapping algorithms developed by *Hooper and Zebker* [2007] require pixels that persist throughout the time spanned by the images. We expect to relax this requirement in future phase unwrapping algorithms but, for now, we avoid picking these pixels; we estimate the variance of γ_x for each pixel using the bootstrap percentile method [*Efron and Tibshirani*, 1986] with 1000

iterations, and drop pixels with a standard deviation over a defined threshold, a typical value being 0.1.

4.2. Multiple Pixel PS

[50] A scatterer that is bright can dominate pixels other than the pixel corresponding to its physical location. The error in look angle and squint angle due to the offset of the pixel from the physical location usually results in these pixels not being selected as PS pixels. However, for pixels immediately adjacent to the PS pixel the error may be sufficiently small that the pixel appears stable. To avoid picking these pixels, we assume that adjacent pixels selected as PS pixels are due to the same dominant scatterer. As we expect the pixel that corresponds to the physical location to have the highest SNR, for groups of adjacent stable pixels we select as the PS pixel only the pixel with the highest value of γ_x.

5. Displacement Estimation

[51] Once we have selected the most likely PS pixels, we discard all other pixels and return to the original wrapped interferogram phase, $\psi_{x,i}$ (equation (10)). In order to retrieve the phase due to deformation, $\phi_{D,x,i}$, the phase must be unwrapped and other nuisance terms estimated.

5.1. Phase Unwrapping

[52] If no assumptions are to be made about the underlying phase signal, accurate unwrapping is only possible when the absolute difference in phase between neighboring PS pixels is generally less than π. For the spatially correlated part of the signal, this will be true as long as the spatial sampling of the signal by the PS pixels is sufficiently dense. Even when the sampling density is high, the contribution to the absolute difference in phase between neighboring PS pixels can still be greater than π due to the spatially uncorrelated part of the signal. The most significant contribution to this part is the spatially uncorrelated part of the look angle error, $\Delta\phi_\theta^u$, for which we already have an estimate. We also have an estimate for the contribution of the master to the spatially uncorrelated part of the signal, $\widehat{\phi}_x^{m,u}$. We therefore subtract our estimates for these two terms before unwrapping, yielding

$$W\left\{\psi_{x,i} - \Delta\widehat{\phi}_{\theta,x,i}^u - \widehat{\phi}_x^{m,u}\right\}$$
$$= W\left\{\phi_{D,x,i} + \Delta\phi_{A,x,i} + \Delta\phi_{S,x,i} + \Delta\phi_{\theta,x,i}^c + \Delta\phi_{N,x,i}\right\}, \quad (22)$$

where $\Delta\phi_{\theta,x,i}^c$ is the spatially correlated part of $\Delta\phi_{\theta,x,i}$, and $\Delta\phi_{N,x,i}$ is the residual spatially uncorrelated noise term, $\phi_{N,x,i} - \widehat{\phi}_x^{m,u}$.

[53] One strategy for unwrapping this phase is to unwrap spatially the phase difference between each neighboring (in time) pair of interferograms, as done by *Hooper et al.* [2004]. However, as we have three dimensions of phase data, two in space and one in time, more reliable results can be obtained using one of the three-dimensional unwrapping algorithms described by *Hooper and Zebker* [2007]. Whichever algorithm is chosen, the results of unwrapping can be summarized as

$$\widehat{\phi}_{x,i} = \phi_{D,x,i} + \phi_{A,x,i} + \Delta\phi_{S,x,i} + \Delta\phi_{\theta,x,i}^c + \Delta\phi_{N,x,i} + 2k_{x,i}\pi, \quad (23)$$

Table 1. Descending Orbit Data Processed for Alcedo (Track 140, Frame 3620)[a]

Orbit	Date	Sensor	$B_\perp$, m	f_{DC}, Hz
4794	1992-06-15	ERS-1	616	−301.24
13020	1997-10-16	ERS-2	176	−677.10
18531	1998-11-05	ERS-2	533	−574.81
19032	1998-12-10	ERS-2	−917	−633.35
19533	1999-01-14	ERS-2	−484	−574.48
20034	1999-02-18	ERS-2	976	−447.77
20535	1999-03-25	ERS-2	−407	−472.20
25044	2000-02-03	ERS-2	0	−551.03
25545	2000-03-09	ERS-2	−198	−421.53
26046	2000-04-13	ERS-2	−274	−684.07
26547	2000-05-18	ERS-2	−308	−594.90
27048	2000-06-22	ERS-2	−453	−746.82
27549	2000-07-27	ERS-2	−39	−667.34
28551	2000-10-05	ERS-2	−337	−883.46
29052	2000-11-09	ERS-2	−99	−908.65

[a]$B_\perp$ is the perpendicular baseline relative to the master acquisition on 3 February 2000, and f_{DC} is the absolute Doppler centroid.

where $\widehat{\phi}_{x,i}$ is the unwrapped value of $W\{\psi_{x,i} - \Delta\widehat{\phi}^u_{\theta,x,i} - \widehat{\phi}^{m,u}_x\}$ and $k_{x,i}$ is the remaining unknown integer ambiguity. The value of $k_{x,i}$ includes an integer ambiguity associated with each interferogram as a whole, which is not estimated. If the unwrapping is sufficiently accurate, $k_{x,i}$ will be the same integer for most x in a given interferogram i.

5.2. Spatially Correlated Nuisance Terms

[54] After unwrapping, several terms remain in equation (23) that mask $\phi_{D,x,i}$. The spatially uncorrelated part of these nuisance terms can be modeled as noise in any subsequent deformation modeling, but the spatially correlated parts can bias the results, so we seek to estimate and subtract them. We separate the spatially correlated part of the nuisance terms into the part that is correlated in time and the part that is expected not to be. The former consists of the master contribution to $(\phi_{A,x,i} + \Delta\phi_{S,x,i})$, which is present in every interferogram, and the latter consists of the slave contribution to $(\phi_{A,x,i} + \Delta\phi_{S,x,i})$ and $\Delta\phi^c_\theta,x,i$. We estimate both parts separately using a combination of temporal and spatial filtering as described below.

[55] In order to estimate the master contribution to the spatially correlated phase we low-pass filter in time. Because of the whole interferogram contribution to $k_{x,i}\pi$ in equation (23), which is not estimated, absolute values of $\widehat{\phi}_{x,i}$ are essentially decorrelated in time and we are not able to apply a temporal filter directly. However, $k_{x,i}$ is identical for most neighboring PS pixels; thus calculating the phase differences between neighboring PS pixels cancels the $2k_{x,i}\pi$ term in most cases, and the resulting phase can be filtered. We first form a spatial network connecting all PS pixels using Delaunay triangulation. In each interferogram we difference $\widehat{\phi}_{x,i}$ between pairs of PS pixels around each triangle, in a clockwise direction, giving (from equation (23))

$$\Delta_{x_1}^{x_2}\widehat{\phi}_{x,i} = \Delta_{x_1}^{x_2}\phi_{D,x,i} + \Delta_{x_1}^{x_2}\phi_{A,x,i} + \Delta_{x_1}^{x_2}\Delta\phi_{S,x,i}$$
$$+ \Delta_{x_1}^{x_2}\Delta\phi^c_{\theta,x,i} + \Delta_{x_1}^{x_2}\Delta\phi_{N,x,i}, \tag{24}$$

where $\Delta_{x_1}^{x_2}$ is the phase differencing operator between PS pixels x_2 and x_1. For each PS pair, we low-pass filter the

differenced phase in time by convolution with a Gaussian function yielding

$$\mathcal{L}^T\{\Delta_{x_1}^{x_2}\widehat{\phi}_i\} \approx \Delta_{x_1}^{x_2}\phi_{D,i} - \Delta_{x_1}^{x_2}\phi^m_A - \Delta_{x_1}^{x_2}\Delta\phi^m_S, \tag{25}$$

where $\mathcal{L}^T\{\cdot\}$ is the low-pass filter operator, and superscript m indicates the master contribution to these terms. The width of the Gaussian is chosen to be less than the time over which deformation rate is expected to vary, in order to preserve the deformation phase. Evaluating $\mathcal{L}^T\{\Delta_{x_1}^{x_2}\widehat{\phi}_i\}$ at the master time, when $\phi_{D,x} = 0$ for all x, gives an estimate for $(\Delta_{x_1}^{x2}\phi^m_A + \Delta_{x_1}^{x2}\Delta\widehat{\phi}^m_S)$. The estimate, $(\widehat{\phi}^m_{A,x} + \Delta\widehat{\phi}^m_{S,x})$ with respect to an arbitrary reference PS pixel is retrieved by least squares inversion.

[56] In order to estimate the slave contributions to the spatially correlated phase, which are expected to be temporally uncorrelated, we apply a high-pass filter in time to the phase difference between neighboring PS pixels, $\Delta_{x_1}^{x2}\widehat{\phi}_i$. We achieve this by subtracting the low-pass-filtered signal, $\mathcal{L}^T\{\Delta_{x_1}^{x2}\widehat{\phi}_i\}$, giving (from equations (25) and (24))

$$\Delta_{x_1}^{x2}\widehat{\phi}_i - \mathcal{L}^T\left\{\Delta_{x_1}^{x2}\widehat{\phi}_i\right\}$$
$$\approx \Delta_{x_1}^{x2}\phi^s_{A,i} + \Delta_{x_1}^{x2}\Delta\phi^s_{S,i} + \Delta_{x_1}^{x2}\Delta\phi^c_{\theta,i} + \Delta_{x_1}^{x2}\Delta\phi_{N,i}, \tag{26}$$

where superscript s indicates the slave contribution to these terms. For each interferogram the high-pass-filtered signal for each PS pixel, with respect to an arbitrary reference PS pixel, is retrieved from equation (26) by least squares inversion,

$$\left[\Delta_{x_1}^{x_2}\right]^{-1}\left\{\Delta_{x_1}^{x_2}\widehat{\phi}_i - \mathcal{L}^T\left\{\Delta_{x_1}^{x_2}\widehat{\phi}_i\right\}\right\}$$
$$\approx \phi^s_{A,x,i} + \Delta\phi^s_{S,x,i} + \Delta\phi^c_{\theta,x,i} + \Delta\phi_{N,x,i}, \tag{27}$$

where $[\Delta_{x_1}^{x2}]^{-1}$ is the inverse phase differencing operator with respect to the reference PS pixel. We then low-pass filter this phase spatially, for each interferogram, by convolution with a two-dimensional Gaussian function. We wish to include all of the signal except for that localized to individual PS pixels, so we set the width of the Gaussian

Table 2. Ascending Orbit Data Processed for Alcedo (Track 61, Frame 7176)[a]

Orbit	Date	Sensor	$B_\perp$, m	f_{DC}, Hz
17951	1998-09-26	ERS-2	−650	29.46
18452	1998-10-31	ERS-2	−707	−92.33
19955	1999-02-13	ERS-2	−854	−71.67
20456	1999-03-20	ERS-2	−707	−25.25
24965	2000-01-29	ERS-2	0	25.39
25466	2000-03-04	ERS-2	298	−184.15
25967	2000-04-08	ERS-2	387	−193.15
26468	2000-05-13	ERS-2	−900	592.97
26969	2000-06-17	ERS-2	−733	500.57
27470	2000-07-22	ERS-2	33	274.85
28472	2000-09-30	ERS-2	122	517.95
28973	2000-11-04	ERS-2	370	143.69
29474	2000-12-09	ERS-2	57	446.37
29975	2001-01-13	ERS-2	−726	−176.83

[a]$B_\perp$ is the perpendicular baseline relative to the master acquisition on 29 January 2000 and f_{DC} is the absolute Doppler centroid.
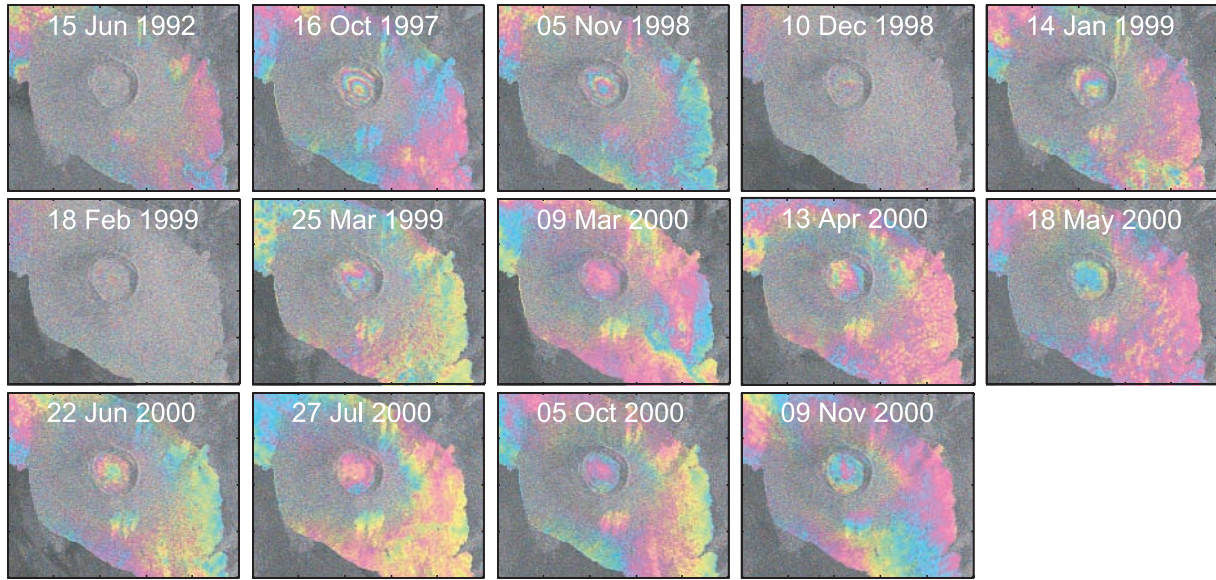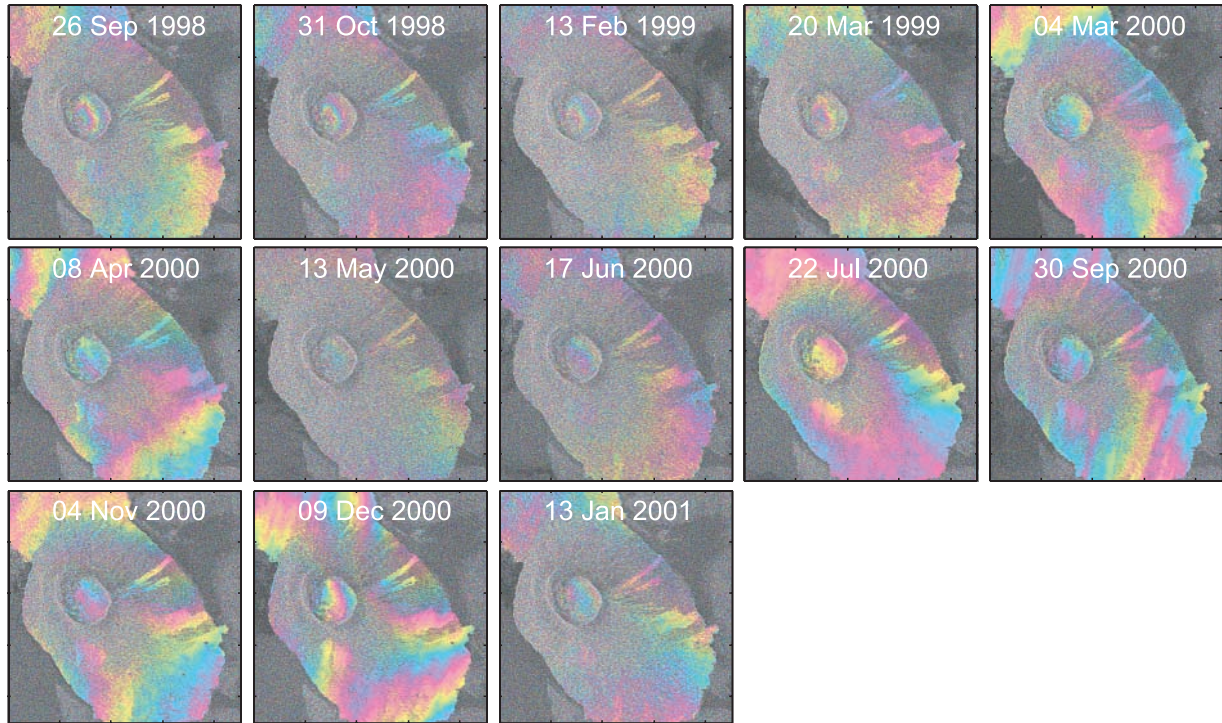
Figure 6. Wrapped interferograms in radar coordinates formed from descending orbit data acquired over Alcedo, with 4 looks taken in range and 20 in azimuth. The master acquisition date is 3 February 2000. Each color fringe represents 2.8 cm of displacement in the LOS, and the intensity reflects interferogram amplitude.

to be narrow, typically 50 m. The output from the spatial filter provides an estimate of $\left(\widehat{\phi}_{A,x,i}^{s} + \Delta\widehat{\phi}_{S,x,i}^{s} + \Delta\widehat{\phi}_{\theta,x,i}^{c}\right)$. Rearranging equation (23) and substituting in the terms estimated in this section gives

$$
\phi_{D,x,i} - \Delta\phi_{N,x,i} - 2k_{x,i}\pi
$$
$$
\approx \widehat{\phi}_{x,i} + \left(\widehat{\phi}_{A,x}^{m} + \Delta\widehat{\phi}_{S,x}^{m}\right) - \left(\widehat{\phi}_{A,x,i}^{s} + \Delta\widehat{\phi}_{S,x,i}^{s} + \Delta\widehat{\phi}_{\theta,x,i}^{c}\right).
$$

$$(28)$$

Figure 7. Wrapped interferograms in radar coordinates formed from ascending orbit data acquired over Alcedo, with 4 looks taken in range and 20 in azimuth. The master acquisition date is 29 January 2000. Each color fringe represents 2.8 cm of displacement in the LOS, and the intensity reflects interferogram amplitude.

Table 3. Parameters Used in the StaMPS Processing of Alcedo Data

Parameter	Value
DEM	SRTM 3 arc sec
Maximum DEM error	10 m
Band-pass phase filter grid cell size	40 m
Band-pass phase filter grid size	64 × 64
Band-pass phase filter low-pass cutoff	800 m
Band-pass phase filter α	1
Band-pass phase filter β	0.3
Acceptable fraction of false positive PS pixels	1%
Partial PS pixels rejected?	no
Spatially correlated filtering time window	180 days
Spatially correlated filtering minimum wavelength	50 m
Unwrapping algorithm	stepwise 3-D
Unwrapping grid cell size	100 m
Unwrapping Gaussian width	8σ

[57] Typically, we consider the resultant phase relative to some small region of the image, which cancels the whole interferogram contribution to the $2k_{x,i}\pi$ term, and leaves phase due only to deformation, spatially uncorrelated noise and unwrapping errors.

[58] In practice, it is possible that the spatially correlated nuisance terms may also be correlated temporally, in which case they will not be correctly estimated by the procedure described above. For the atmospheric term, this may be the case in regions where tropospheric moisture content varies seasonally, as in coastal areas where fog is more prevalent at certain times of the year. Further processing is required if this is suspected to be the case. For the orbit error term, we have found with data from the Radarsat-1 satellite that values can be large and, apparently by chance, correlated in time. This is not the case for the Volcán Alcedo data we analyze in section 6, but when this does occur, phase ramps can be removed from interferograms where the orbit error term is visible before estimating the other spatially correlated terms. Extra care should then be taken in interpreting the deformation signal, as any overall tilt signal will be removed by this procedure, and residual nonlinear contributions to the orbit error term will remain [*Kohlhase et al.*, 2003].

[59] Care should also be taken if the number, or distribution, of interferograms is such that they sample the signal in time at a rate that is too low to capture the detailed variation in deformation rate. Some of the deformation signal may then leak into the estimate for the spatially correlated nuisance terms, which may be visible as a recurring spatial pattern in the estimate of these terms for each interferogram.

6. Application to Volcán Alcedo

[60] We applied StaMPS to data acquired by ERS-1 and ERS-2 satellites over Volcán Alcedo between June 1992 and
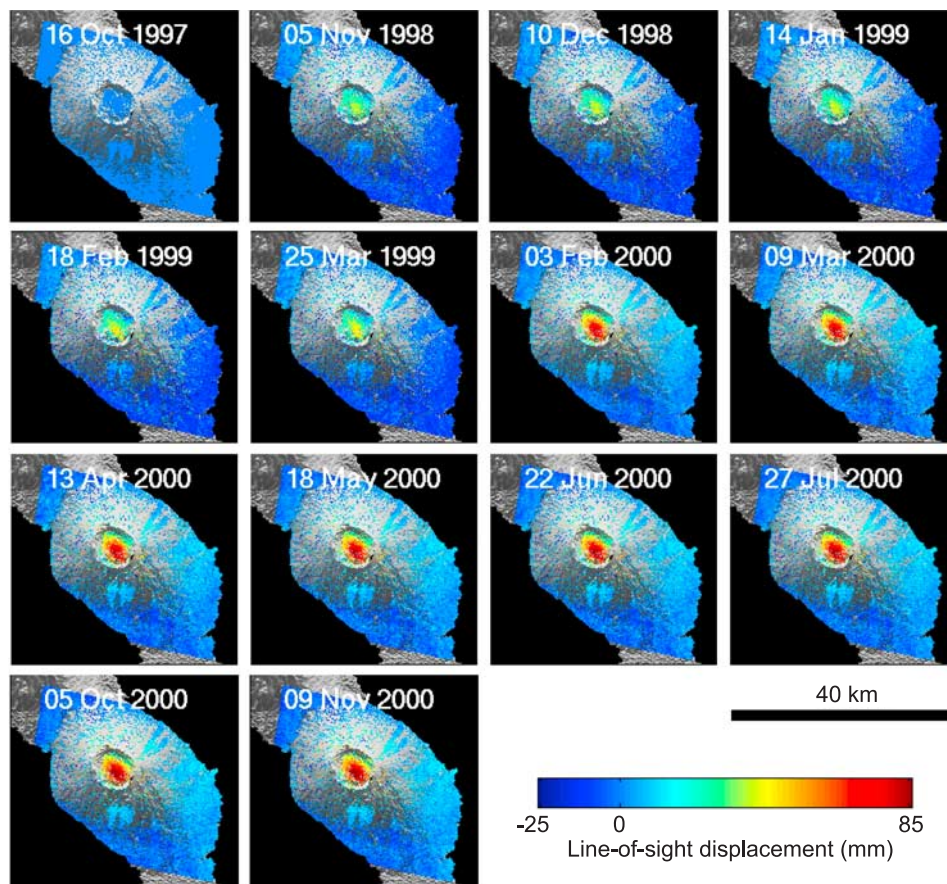

Figure 8. Descending orbit PS interferograms for Alcedo, plotted on SRTM topography displayed in shaded relief. The data are unwrapped, and spatially correlated error estimates have been subtracted. Displacements are given relative to PS pixels in the southeast and 16 October 1997.
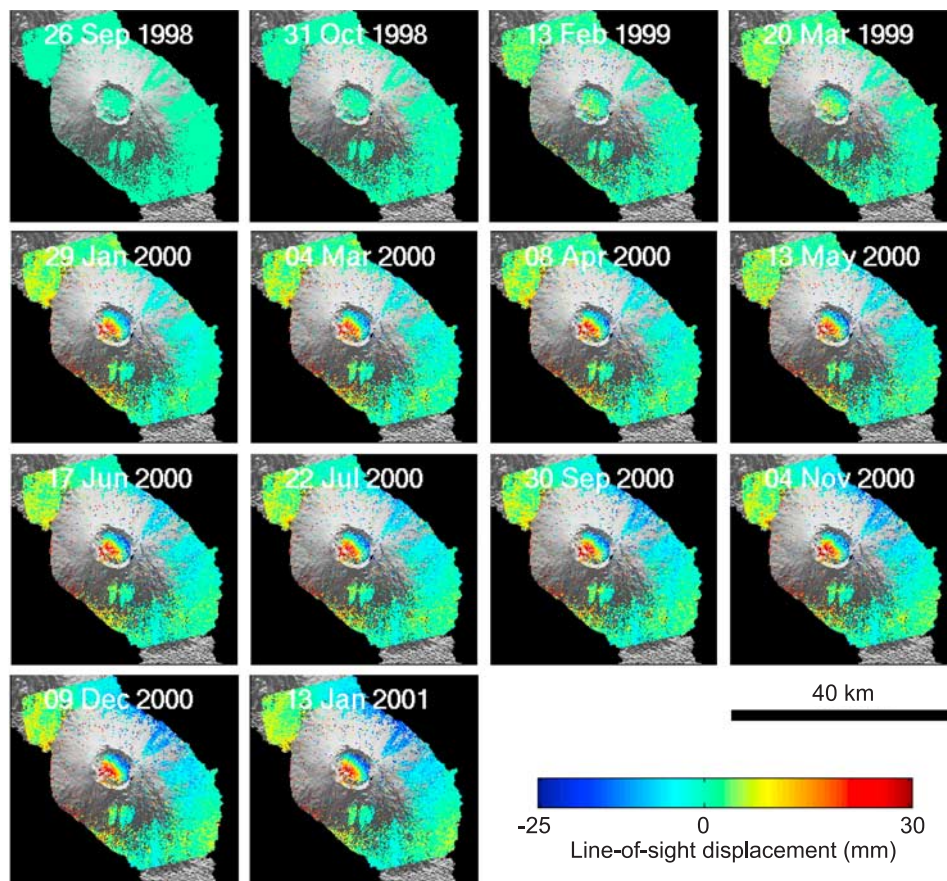
Figure 9. Ascending orbit PS interferograms for Alcedo, plotted on SRTM topography displayed in shaded relief. The data are unwrapped, and spatially correlated error estimates have been subtracted. Displacements are given relative to PS pixels in the southeast and 26 September 1998.

January 2001 (see Tables 1 and 2). Starting from the raw SAR data, the total CPU time we required was approximately four days, using a PC with a 1.5 GHz CPU and 1 GB of RAM. We processed 15 descending track images giving 14 interferograms, each with February 2000 as the reference master image (Figure 6). We also processed 14 ascending track images giving 13 interferograms, each with January 2000 as the reference master image (Figure 7). We used a DEM determined by the Shuttle Radar Topography Mission (SRTM), with a posting of three seconds of arc. The specific parameters we used in the processing are detailed in Table 3. The broad distribution of PS pixels is similar in both the descending and ascending cases, although the positions of individual PS pixels are not necessarily identical (Figures 8 and 9). In the ascending data, the distribution of perpendicular baselines, $B_\perp$, falls into two distinct clusters separated by 707 m. Coregistration between the two clusters is challenging, leading to more error in $\phi_{N,x,i}$ from misregistration than in the descending case. The Doppler centroid separation is also generally larger in the ascending case, leading to a greater noise contribution from background scatterers. Note also that more long-wavelength atmospheric signal is present in the ascending data than the descending data, presumably related to the difference in acquisition time which is 10.45 p.m., local time, for the ascending orbit as opposed to 10.23 a.m. for the descending orbit.

[61] An event causing asymmetric deformation occurred within the caldera between June 1992 and October 1997 which is visible in the interferogram of *Amelung et al.* [2000]. Although this event is clear in the wrapped phase of the PS pixels in an interferogram covering this time interval (Figure 10), the spatial sampling of the PS pixels is not high enough everywhere to unwrap the signal associated with this event. The spatial pattern of the wrapped phase is, however, consistent with trapdoor faulting, similar to that observed on Sierra Negra [*Amelung et al.*, 2000; *Chadwick et al.*, 2006], another volcano located on Isla Isabela. In the case of Alcedo, the fault appears to be located in the southwest of the caldera, striking approximately northwest-southeast. For all subsequent acquisitions, which cover the time interval between October 1997 and January 2001, we are able to extract and unwrap the deformation signal (Figures 8 and 9).

6.1. Modeling

[62] Our results show a dominant deflation signal for the entire 1997 to 2001 time interval, largely confined within the caldera. The rate of deflation appears to be approximately constant over this time interval, and can be observed by the change in maximum LOS displacement in the descending data (Figure 11a). There is also a discontinuity in the displacement rates following the trend of a break in topography on the west side of the caldera. The rate of
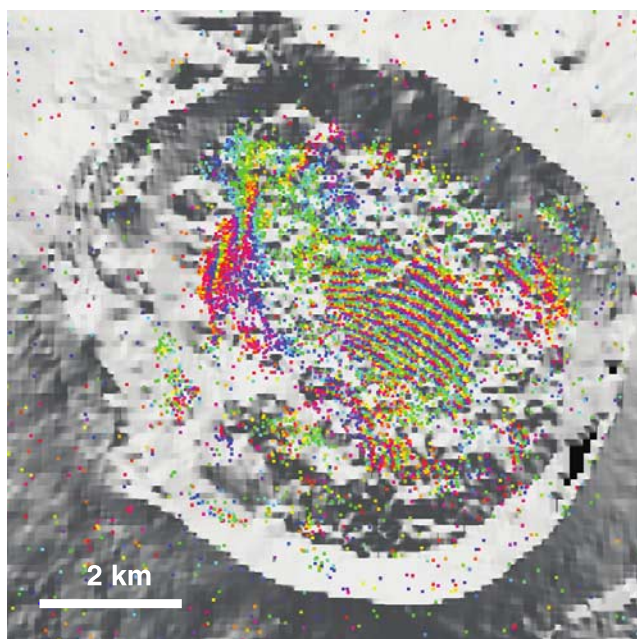
Figure 10. Wrapped PS interferogram for Alcedo caldera covering the interval 15 June 1992 to 5 November 1998. The background image is SRTM topography in shaded relief. Each color fringe represents 2.8 cm of displacement in the LOS, and the southern end of the fringes is moving toward the satellite with respect to the northern end.

deformation to the west of this discontinuity also appears be approximately constant as observed by the change in LOS displacement between the west side and east side of the caldera in the ascending data (Figure 11b). Both modes of deformation appear to be constant in rate, and we calculate the mean LOS velocities for each PS pixel in both the descending and ascending data. For the descending data we are able to refer the velocities to the mean signal at the coasts (Figure 12), which we assume to be unaffected by the local deformation detected here and moving at the tectonic plate velocity. For the ascending data, unwrapping between the caldera and the coast is unreliable due to the higher phase noise; therefore we analyze only the data within the caldera and refer the velocities to the east side of the caldera (Figure 13).

[63] PS pixels on the west side of the caldera that seem most affected by the second mode of deformation are located on the inner slope of the caldera (see topography in Figure 13). Relative to the velocities expected from the deflationary signal alone, in the ascending data, PS pixels on the slopes are moving away from the satellite and, in the descending data, they are moving toward the satellite. This implies a horizontal component of deformation. Given that there is a sharp change in velocities moving from the slopes to the caldera floor, we interpret this mode of deformation as landsliding.

[64] The similarity between Alcedo and Sierra Negra, in terms of evidence of trapdoor faulting, might lead us to assume similar geometries for their shallow magma chambers. Deformation on Sierra Negra between September 1998 and March 1999 can be fit well by an inflating sill-like body

situated entirely within the caldera boundaries and about 2 km below the surface [*Amelung et al.*, 2000; *Jónsson*, 2002; *Yun et al.*, 2006]. However, for Alcedo, the offset in the position of maximum LOS velocity on the caldera floor between ascending and descending geometries (Figures 12 and 13) indicates that there is significant horizontal displacement, more consistent with a three-dimensional source than a sill-like body. The asymmetry of the deformation pattern suggests that the source is not radially symmetrical, so we model it with a contracting, finite ellipsoid [*Yang et al.*, 1988]. We use only the velocities of PS pixels located on the caldera floor to avoid bias in our results from the second mode of deformation. The caldera is essentially flat and we approximate it with a half-space. We assume a shear
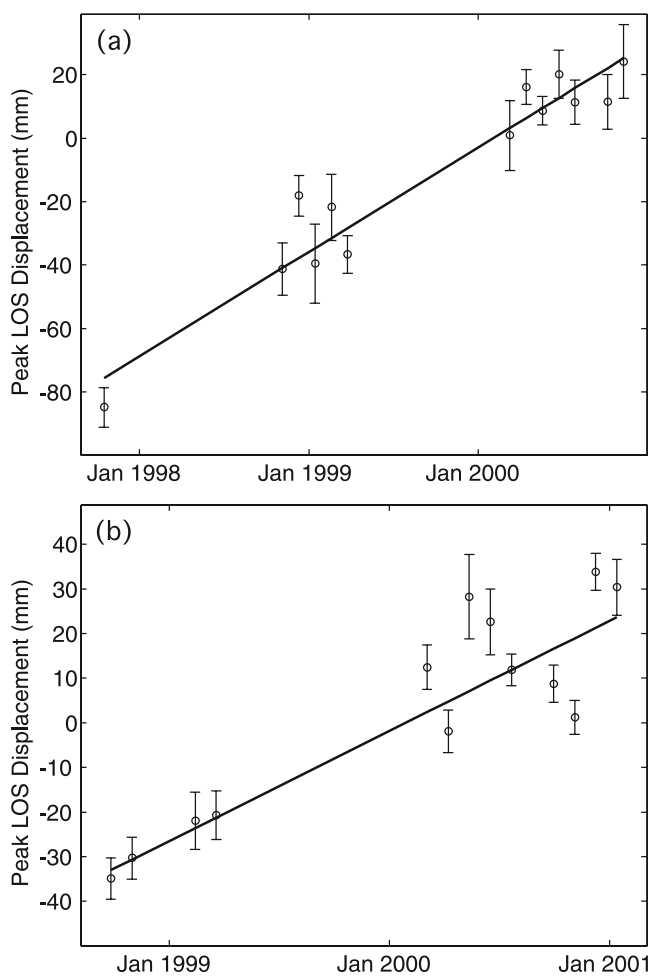

Figure 11. Maximum LOS displacements on Alcedo for (a) descending orbit and (b) ascending orbit data.. For each PS interferogram the mean LOS displacement of the region of maximum displacement is plotted. For the descending case the displacements are relative to PS pixels near the coasts and for the ascending case the displacements are relative to PS pixels on the east side of the caldera. Error bars represent one sample standard deviation. To avoid any bias caused by temporal smoothing, the displacements are calculated before spatially correlated terms are subtracted, which causes extra scatter. Also plotted is the best fitting constant LOS velocity in each case.
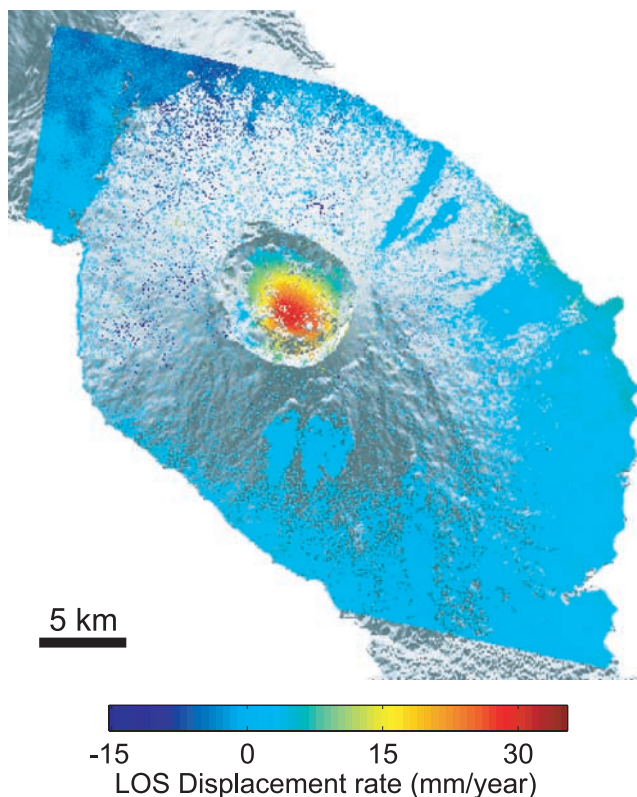
Figure 12. Mean LOS velocities on Alcedo between October 1997 and November 2000 from descending orbit data. The velocities are relative to the mean velocity of PS pixels on the coasts.

modulus of 30 GPa, with no change in rheology to the depth of the deformation source, and also assume that the volcano deforms as a Poisson solid.

[65] Using both descending and ascending LOS velocities, Markov chain Monte Carlo sampling enables us to find the posterior probability distribution of the model parameters [*Mosegaard and Tarantola*, 1995]. We assume zero velocity at the coasts in the descending data. For the ascending data we estimate an additional velocity offset for the east side of the caldera. We also assume that the probability density of the velocities approximates a multivariate Gaussian distribution. Several randomly chosen marginal distributions of the data, estimated using the percentile bootstrap method of *Efron and Tibshirani* [1986], suggest this to be a reasonable assumption (Figure 14).

[66] We reduce the data to a manageable size for computing purposes by resampling both descending and ascending data sets to a 90 m grid. We combine velocities for PS pixels within the same grid cell by taking the weighted mean, using $1/\widehat{\sigma}_{rate,x}$ as the weight for each pixel, where $\widehat{\sigma}^2_{rate,x}$ is the estimated variance of the velocity distribution for pixel x. We estimate this distribution for each PS pixel using the percentile bootstrap method [*Efron and Tibshirani*, 1986] to recalculate velocity 1000 times. The position we assign to each grid cell is the weighted mean position of all PS pixels within the cell. The variance-covariance matrix for each of our reduced data sets also follows from the percentile bootstrap method.
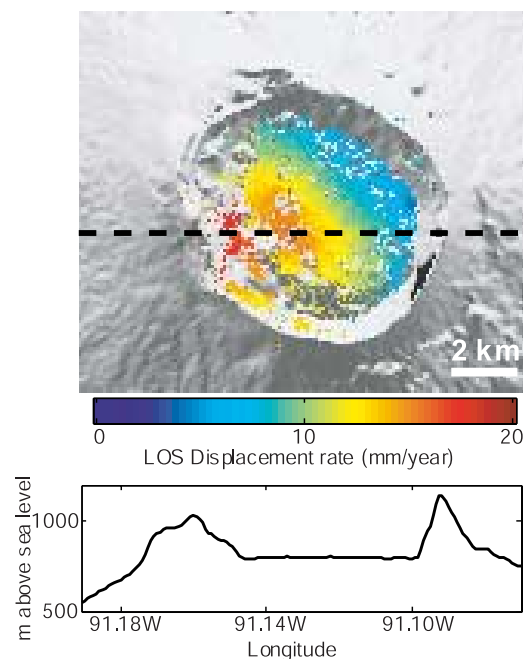

Figure 13. Mean LOS velocities in Alcedo Caldera between September 1998 and January 2001 from ascending orbit data. The velocities are relative to the mean velocity of PS pixels on the east side of the caldera. Also shown is the SRTM elevation for an east–west transect through the caldera.

[67] The probability density function that we use as our prior distribution for each reduced data set is given by

$$P(x) = \frac{exp\left\{-\frac{1}{2}(\boldsymbol{x}-\boldsymbol{\mu})^T\boldsymbol{\Sigma}^{-1}(\boldsymbol{x}-\boldsymbol{\mu})\right\}}{\sqrt{(2\pi)^n|\boldsymbol{\Sigma}|}}, \qquad (29)$$
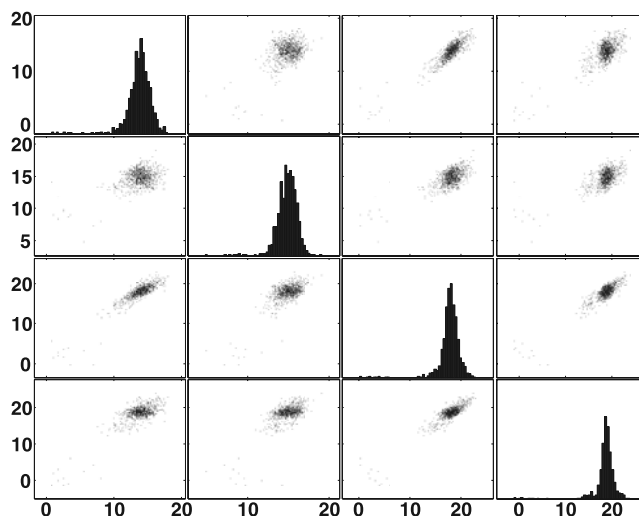

Figure 14. Marginal probability distributions of LOS velocity, in mm/year, for four randomly chosen PS pixels. The histograms show the distributions for each individual PS pixel, and the scatterplots show the distributions for each pair of PS pixels.
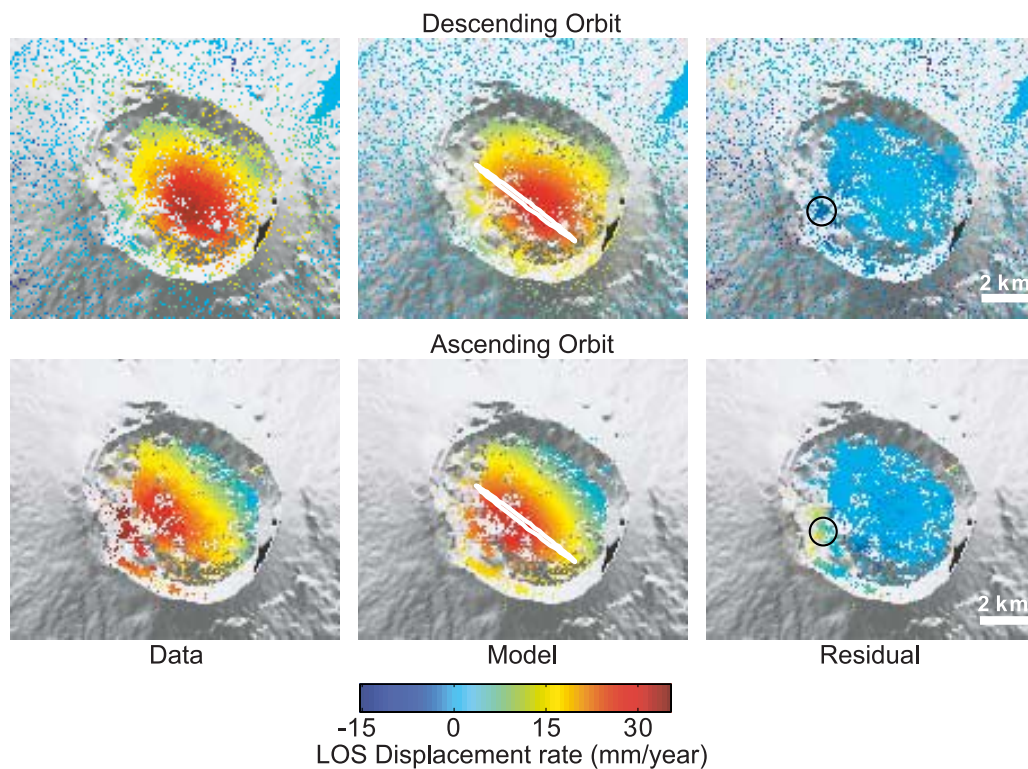
Figure 15. Maximum likelihood model for PS pixels on the caldera floor. The LOS velocities of PS pixels are shown, together with the velocities predicted by the model and the residual between the two. The ellipse overlaying the predicted velocities is the surface projection of the maximum likelihood ellipsoid contracting source. The circle overlaying the ascending data marks the location of the PS pixels used for landslide analysis in section 6.2.

where x is the data vector, μ is the mean vector, n is the number of data, Σ is the variance-covariance matrix and superscript T denotes the transpose. In order to regularize Σ, we increase the diagonal variance terms by 10%. This broadens the marginal probability density function for each grid cell by 10%, which we expect to broaden the posterior model distribution by a negligible amount.

6.2. Results

[68] The maximum likelihood model is shown in Figure 15, together with the LOS velocities predicted by this model, along with the residual difference between these and the data. Although only velocities for PS pixels on the floor of the caldera are used in the inversion, the predicted velocities are shown for all PS pixels. Residual velocities for PS pixels located on the inner slopes of the caldera are assumed to be due to landsliding. The root-mean-square residual value for the PS pixels used in the inversion is 1.9 mm yr^{-1}.

[69] We plot marginal probability densities from Markov chain Monte Carlo sampling, for all the model parameters except position, in Figure 16. The depth of the source is well constrained, lying between 2.21 and 2.26 km below sea level at 95% confidence, with the best fit at 2.24 km. This is based on our assumption of constant shear modulus, however. If shear modulus actually increases with depth, as is usually the case, we might expect the depth range to be somewhat deeper. Although the semimajor axis of the source ellipsoid is well constrained, between 2.5 and 2.7 km at 95%

confidence, the aspect ratio is less well constrained. The maximum likelihood model (shown in Figure 15) is very prolate, with an aspect ratio of 25.5, but an aspect ratio of 5.7 would also fit the data at 95% confidence. The volume decrease is well constrained, between 1.25 and 1.30 × 10^6 m^3 at 95% confidence, with a clear trade-off with both the depth and semiminor axis of the ellipsoid source. The strike of the ellipsoid lies between 127° and 128° and the dip is subhorizontal, dipping upward between 1.3 and 4.7° at 95% confidence.

[70] In order to determine the motion due to landsliding, we resolve the residual velocities, after subtraction of the deflationary source, into eastward and subvertical components. The subvertical component includes a small component of any northward motion. For the PS pixels lying within the circles marked on the residual plots in Figure 15, the eastward component is between 6.5 and 6.7 mm/year and the subvertical component is between 2.3 and 2.7 mm/year downward. This corresponds to an eastward plunge of between 19.4° and 21.9° for the motion.

7. Geophysical Interpretation

[71] Although the data are reasonably well fit by an ellipsoidal source, in all likelihood, the geometry is more complex. However, it appears that the source of the deflation is not equidimensional, and that the longest axis runs subparallel with the long axis of Isla Isabela in the region of Alcedo. If we assume that the source represents a
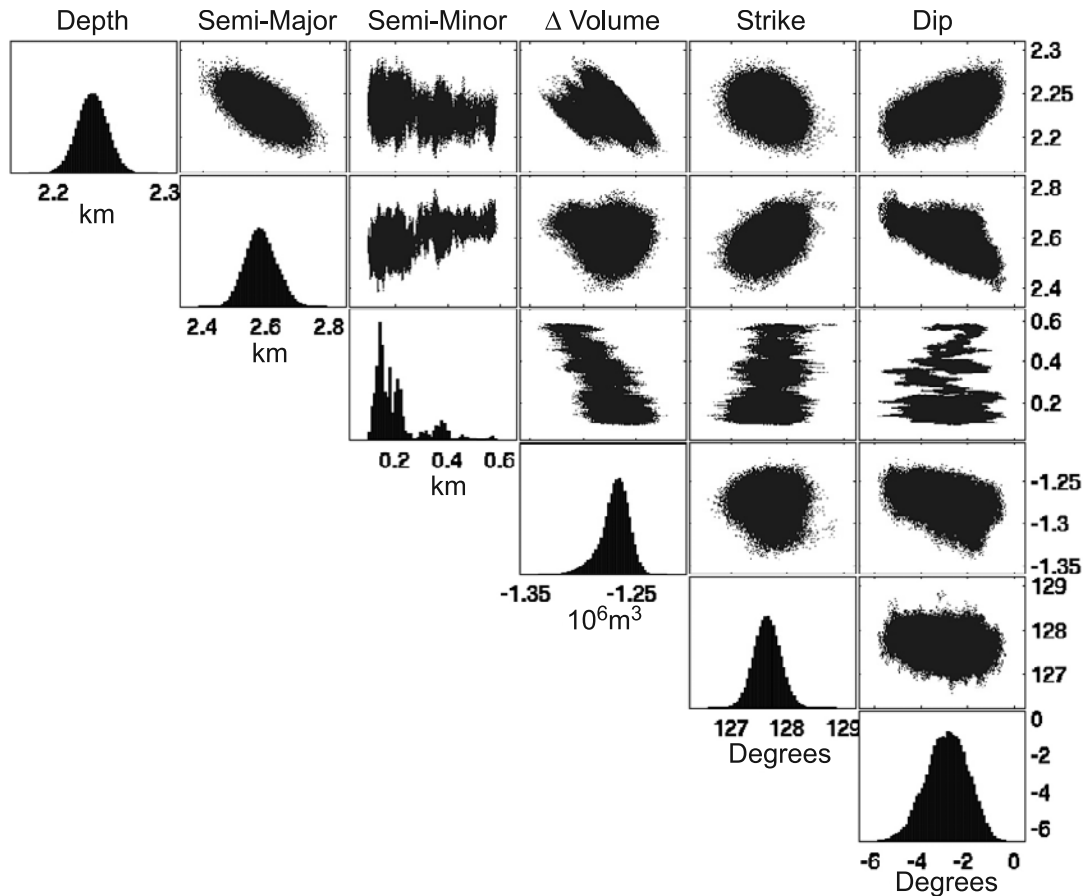
Figure 16. Marginal posterior probability distributions for ellipsoidal source model parameters. The histograms show the distributions for individual parameters and the scatterplots show distributions for each pair of parameters.

preexisting magma chamber, the shape and orientation of the chamber imply that the axis of least compressive stress runs approximately southwest-northeast. The bathymetry of the region (Figure 17) shows a raised platform on all sides of Alcedo except to the northeast, where the depth drops rapidly from 500 m to 2500 m within 10 km. Thus we might expect the least resistance to intrusion to be oriented toward the northeast.

[72] There was no known eruption during this time interval, so the most likely causes of the deflation are contraction due to crystallization and cooling, and the loss of volatiles from the source area. Crystallization of magma emplaced at 3 km beneath the Krafla central volcano in Iceland was estimated to result in a reduction in volume of ~9% [*Sigmundsson et al.*, 1997]. If we assume a similar value for magma emplaced beneath Alcedo, between 0.6 and 10% of the magma would need to crystallize each year, to give the model distribution of volume reduction at 95% confidence. Note that the probability distribution for percentage of crystallization is less well constrained than that for volume reduction, as it also depends on the total volume which is not so well constrained. Cooling of the solidified magma could also contribute further to the volume reduction, with up to 2% contraction being the estimated value for solidified Krafla magma. Loss of volatiles from the magma chamber would reduce the pressure, also leading to

a reduction in volume, but the pressure decrease required to produce the surface displacements would be between 23 and 370 MPa yr^{-1} at 95% confidence. This range is too high to be plausibly produced by the loss of volatiles alone.

[73] The local eastward slope dip for the PS pixels circled in Figure 15 is 15.7°. Our estimate of the dip of the landsliding motion is somewhat steeper, which suggests that there is additional vertical settling. Given that the displacements we measure are those of the dominant scatterers within each pixel, which are most likely the larger boulders in this case, additional settling is possible.

8. Conclusions

[74] We have developed a method to extract the deformation signal from a series of SAR images for pixels whose scattering characteristics vary little with time and look angle (PS pixels). The method works in terrains with or without buildings and no assumptions about variations in displacement rate are required. We refer this method as the Stanford method for persistent scatterers (StaMPS).

[75] Using StaMPS we extract the deformation signal from SAR data acquired over Volcán Alcedo between 1997 and 2001. The signal we find implies deflation of a subhorizontal, prolate ellipsoidal source, extended in the direction of the long axis of Isla Isabela, which is consistent
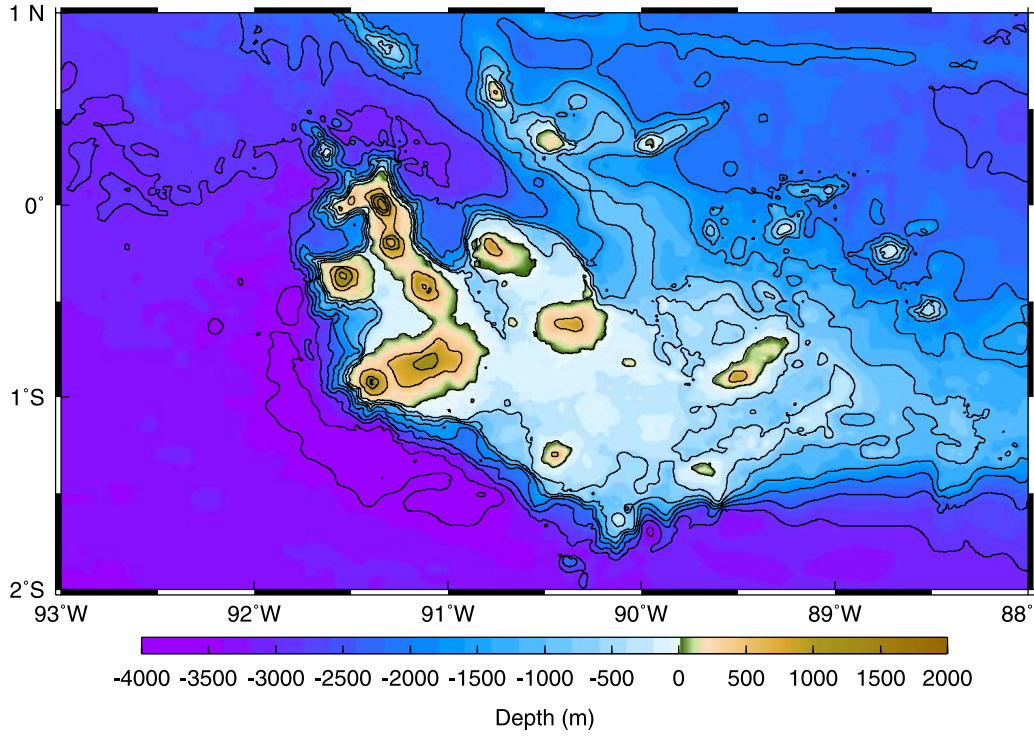
Figure 17. Bathymetry of the Galápagos region, from data compiled by W. Chadwick, Oregon State University. The contour interval is 500 m.

with crystallization of a pipe-like magma body at around 2.2 km depth. We also detect displacements on the inner slopes of the west side of the caldera that are consistent with landsliding.

Appendix A: Coregistration Algorithm

[76] For image m, we define functions $f_x^m(x^m, y^m)$ and $f_y^m(x^m, y^m)$ that map range position $x^m \rightarrow x^0$ and azimuth position $y^m \rightarrow y^0$, respectively, where superscript 0 denotes the master image. For any point k in image m, $f_x^m(x_k^m, y_k^m)$ is equal to the range offset of the point between image m and the master image, $\Delta x_{m,k}^0$, and $f_y^m(x_k^m, y_k^m)$ is equal to the azimuth offset, $\Delta y_{m,k}^0$. We approximate $f_x^m(x^m, y^m)$ as a polynomial function in x^m and y^m,

$$f_x^m(x^m, y^m) \approx a_{00}^m + a_{10}^m x^m + a_{01}^m y^m + a_{11}^m x^m y^m + \cdots + a_{pq}^m (x^m)^p (y^m)^q + \cdots, \tag{A1}$$

where a_{pq}^m represents the coefficient that is pth order in x^m and qth order in y^m. Typically we use terms up to second order. We approximate $f_y^m(x^m, y^m)$ similarly.

[77] When correlation is high between the master and slave images, as is usually the case for conventional InSAR, it is possible to estimate $\Delta \hat{x}_{m,k}^0$ directly at many points, using amplitude cross correlation between the two images. For PS analysis, however, we cannot rely on high correlation between master and slave images. Instead, we estimate offsets, $\Delta \hat{x}_{m,k}^n$, between all pairs of images, m and n, that we expect to be highly correlated. We estimate the offsets using amplitude cross correlation centered on point k, with a typical oversample factor of 32 and a

typical window size of 64 pixels. The offsets between two slave images depend on offsets relative to the master image as

$$\Delta x_{m,k}^n = \Delta x_{m,k}^0 - \Delta x_{n,k}^0$$
$$= f_x^m(x_k^m, y_k^m) - f_x^n(x_k^n, y_k^n), \tag{A2}$$

where $x_k^n = x_k^m + \Delta x_{m,k}^n$ and $y_k^n = y_k^m + \Delta y_{m,k}^n$. We then estimate the coefficients of function $f_x^m(x^m, y^m)$ for all images simultaneously, by solving the following linear system of equations,

$$\begin{bmatrix} \cdots & \cdot & \cdot & \cdot & \cdots & \cdot & \cdot & \cdot & \cdots \\ \cdots & 1 & x_k^m & y_k^m & \cdots & -1 & -x_k^n & -y_k^n & \cdots \\ \cdots & 1 & x_{k+1}^m & y_{k+1}^m & \cdots & -1 & -x_{k+1}^n & -y_{k+1}^n & \cdots \\ \cdots & \cdot & \cdot & \cdot & \cdots & \cdot & \cdot & \cdot & \cdots \end{bmatrix} \begin{bmatrix} \cdot \\ a_{00}^m \\ a_{10}^m \\ a_{01}^m \\ \cdot \\ \cdot \\ a_{00}^n \\ a_{10}^n \\ a_{01}^n \\ \cdot \end{bmatrix}$$
$$= \begin{bmatrix} \cdot \\ \Delta \hat{x}_{m,k}^n \\ \Delta \hat{x}_{m,k+1}^n \\ \cdot \end{bmatrix}, \tag{A3}$$

where there is a row for every offset estimate between all pairs of images that are highly correlated. We use weighted least squares inversion, with the weighting for each estimate being $1/\sigma_{\Delta \hat{x}}$ where $\sigma_{\Delta \hat{x}}$ is the standard deviation of the
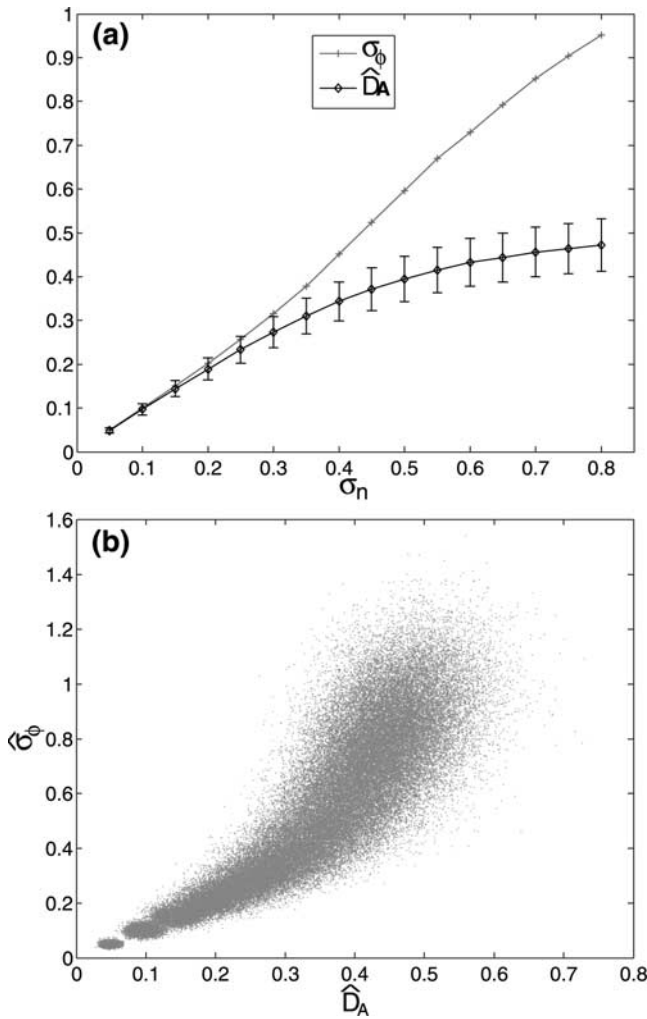
Figure B1. Amplitude dispersion numerical simulation results. The signal model is $z_i = g + n_i$ ($i = 1, \cdots, 34$). The value of g is fixed to 1 while the standard deviation, σ_n, of both the real and imaginary components of the noise, n_i, is incremented from 0.05 to 0.8. For each value of σ_n, we calculate 5000 estimates of $\widehat{D}_A$. (a) Mean values of $\widehat{D}_A$ plotted for each value of σ_n, as by *Ferretti et al.* [2001], with error bars representing one standard deviation. Also plotted are corresponding values of phase standard deviation, σ_ϕ. (b) Same data plotted in a scatterplot of the estimated phase standard deviation, $\widehat{\sigma}_\phi$, versus $\widehat{D}_A$ for all values of σ_n.

estimate $\Delta\widehat{x}$. We estimate $\sigma_{\Delta\widehat{x}}$ from the coherence of the cross correlation, γ, using the formula derived by *Bamler* [2000], which states

$$\sigma_{\Delta\widehat{x}} = \sqrt{\frac{3}{2N}} \frac{\sqrt{1-\gamma^2}}{\pi\gamma} \eta^{3/2}, \qquad (A4)$$

where N is the number of samples in the estimation window and η is the oversampling factor of the data. We find the coefficients of $f_y^m(x^m, y^m)$ similarly.

[78] In order to resample image m into the master coordinate system, the functions we require are actually the inverse functions, $g_x^m(x^0, y^0)$ and $g_y^m(x^0, y^0)$ that map position $x^0 \rightarrow x^m$ and $y^0 \rightarrow y^m$, respectively. We obtain

$g_x^m(x^0, y^0)$ for each image by synthesizing a grid of values of x^m and y^m, estimating $\Delta\widehat{x}_{m,k}^0$ and $\Delta\widehat{y}_{m,k}^0$ from $f_x^m(x^m, y^m)$ and $f_y^m(x^m, y^m)$, and solving for the coefficients of $g_x^m(x^0, y^0)$, b_{pq}^m, by inverting the following system of linear equations,

$$\begin{bmatrix} . & . & . & . & \cdots \\ 1 & x_k^0 & y_k^0 & x_k^0 y_k^0 & \cdots \\ 1 & x_{k+1}^0 & y_{k+1}^0 & x_{k+1}^0 y_{k+1}^0 & \cdots \\ . & . & . & . & \cdots \end{bmatrix} \begin{bmatrix} b_{00}^m \\ b_{10}^m \\ b_{01}^m \\ b_{11}^m \\ . \end{bmatrix} = \begin{bmatrix} . \\ -\Delta\widehat{x}_{m,k}^0 \\ -\Delta\widehat{x}_{m,k+1}^0 \\ . \end{bmatrix}, \quad (A5)$$

where $x_k^0 = x_k^m + \Delta x_{m,k}^0$ and $y_k^0 = y_k^m + \Delta y_{m,k}^0$. We find $g_y^m(x^0, y^0)$ similarly.

Appendix B: Amplitude Dispersion Thresholding

[79] *Ferretti et al.* [2001] show that for a constant signal and high signal-to-noise ratio (SNR), $D_A \approx \sigma_\phi$, where σ_ϕ is the phase standard deviation. They plot the relationship using simulation, which we have repeated in Figure B1. The model consists of a constant signal of amplitude 1, with additive noise selected from a complex circular Gaussian distribution with a characteristic standard deviation σ_n for both the real and imaginary components. Figure B1 shows that given 34 images, $\widehat{D}_A$ is a reasonable proxy for σ_ϕ, for low values of σ_ϕ.

[80] However, Figure B1 might lead one to conclude that $\widehat{D}_A$ is a better proxy for phase stability than it really is, for two reasons. First, the error bars show the variability of $\widehat{D}_A$ for a given value of σ_n, but it is the variability of σ_n for a given value of $\widehat{D}_A$ that is required. Although this variability depends on the chosen distribution of σ_n, which is arbitrary here, we can get an idea of the variability of σ_n for any given value of $\widehat{D}_A$ from Figure B1. For instance, given this simulated distribution of σ_n, $D_A = 0.3$ indicates a range for σ_n of about 0.28 to 0.4 at 68% confidence. Second, although a given value of σ_n implies a particular value of σ_ϕ, the variability in phase for a finite sample is better represented by the standard deviation estimated from each sample, $\widehat{\sigma}_\phi$, which varies about σ_ϕ. In this example, a range for σ_n of 0.28 to 0.4 implies a range for $\widehat{\sigma}_\phi$ of about 0.25 to 0.54, at 68% confidence. Thus, even for a relatively small value of $\widehat{D}_A = 0.3$, the variability in phase stability is rather large. An alternate way to view the relationship between $\widehat{D}_A$ and phase stability is by plotting the same data in a scatter plot as in Figure B1b, where the variability of $\widehat{\sigma}_\phi$ for any given value of $\widehat{D}_A$ is immediately apparent. It is also apparent that although D_A tends to the theoretical limit for the Rayleigh distribution of $\sqrt{(4-\pi)/\pi} \simeq 0.523$, as SNR tends to zero [*Ferretti et al.*, 2001], estimated values of $\widehat{D}_A$ from finite samples can be somewhat greater.

[81] The actual relationship between $\widehat{D}_A$ and $\widehat{\sigma}_\phi$ for any given data set depends on the distribution of SNR within the data set. We can estimate a model distribution of SNR for any given data set from $\widehat{D}_A$, and then use this to build a simulated distribution of $\widehat{\sigma}_\phi$ versus $\widehat{D}_A$. First, we estimate SNR distributions for the data set by applying the model of signal plus circular Gaussian noise. We simulate a distribution of $\widehat{D}_A$ for a range of SNR values, and solve for the weighted sum of individual SNR distributions that best fits the distribution of $\widehat{D}_A$ in the data, using a
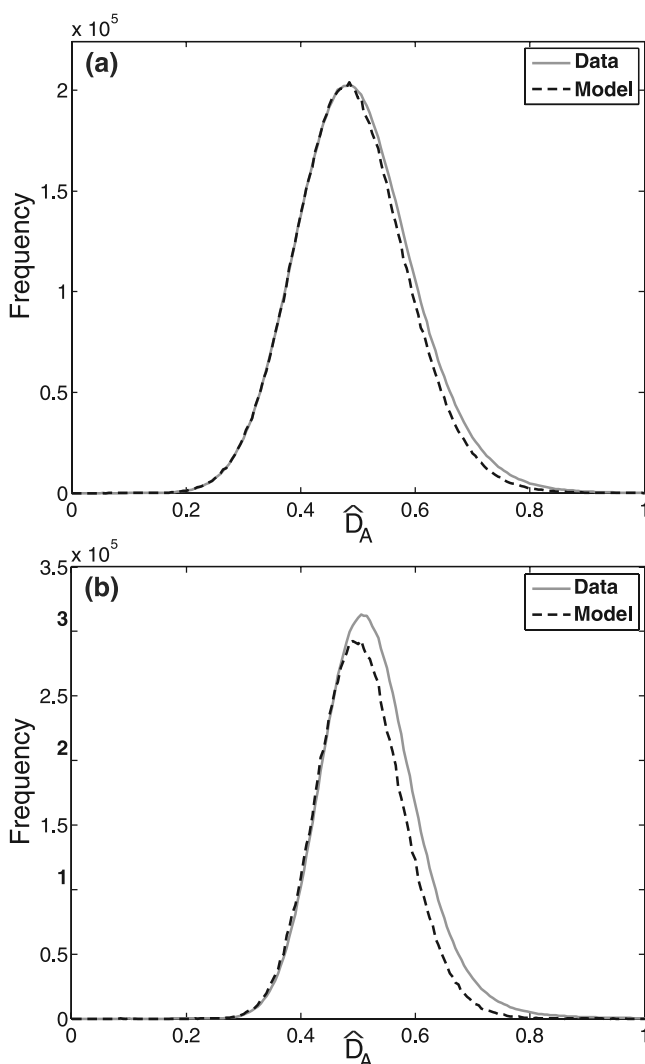
Figure B2. Distribution of amplitude dispersion for (a) 15 images acquired over Volcán Alcedo and (b) 24 images acquired over Mount St. Helens. Also plotted are the distributions predicted from the best fitting model SNR distributions.
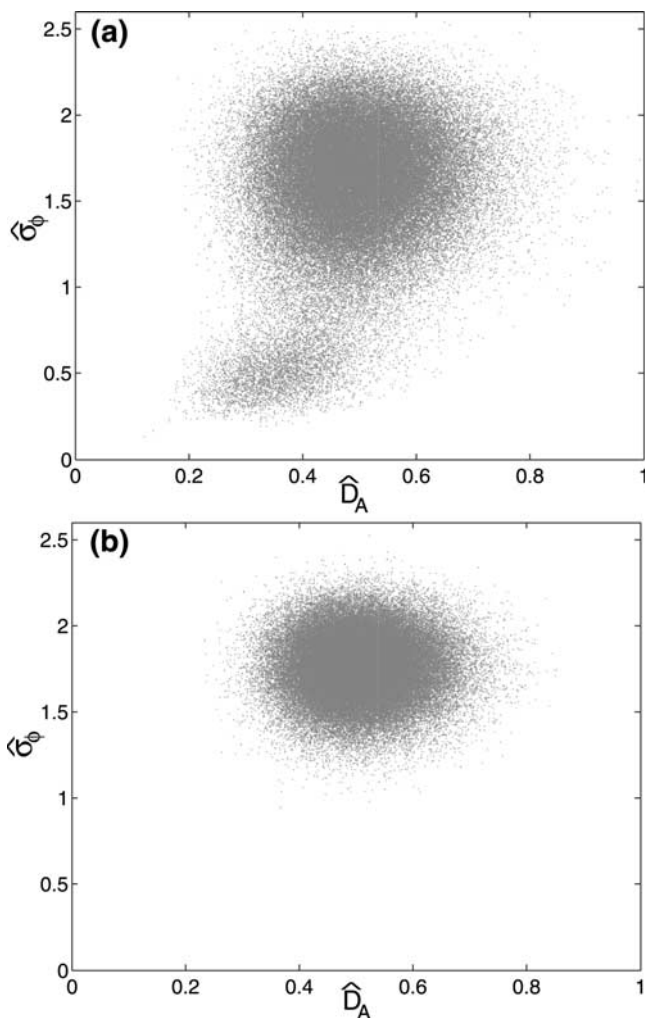
Figure B3. Scatterplots of simulated phase standard deviation versus amplitude dispersion for model distributions of SNR for (a) Volcán Alcedo and (b) Mount St. Helens.

nonnegative least squares algorithm to determine the weightings. Two examples are shown in Figure B2, the first for 15 images acquired over Volcán Alcedo and the second for 24 images acquired over Mount St. Helens in Washington State. Initially, we tried fitting the data for all values of D_A but found for higher values that the model always systematically underfit the data, so we only attempted to fit values of $\widehat{D}_A < 0.5$. The systematic misfit of the data implies that the model does not exactly reflect reality. This was also the conclusion of *Kampes* [2005], who analyzed data acquired over Berlin and found the mean value of $\widehat{D}_A$ to be 0.56. As the maximum theoretical mean value of $\widehat{D}_A$ is 0.523, it is clearly impossible to explain this distribution as the sum of distributions for different SNRs. The underlying assumption of this model is that any pixel can be characterized by fixed SNR in time. As we expect the SNR for some pixels to vary with time, it is not surprising that the model is unable to fit the data distribution exactly. However, for lower values of $\widehat{D}_A$ the model is adequate.

Given our model distributions of SNR, we then simulate the distribution of $\widehat{\sigma}_\phi$ versus $\widehat{D}_A$, as shown in Figure B3. If we took $\widehat{\sigma}_\phi \leq 0.6$ as indicative of phase stability [*Colesanti et al.*, 2003b], simulated values of $\widehat{\sigma}_\phi$ for the Mount St. Helens data set would indicate that there were no stable scatterers at all, according to this definition of phase stability. For the Alcedo data set, the simulated values indicate that even
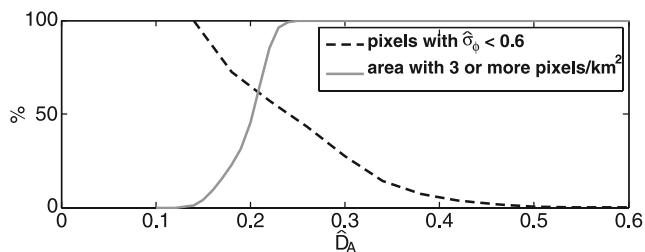
Figure B4. Percentage of high-phase stability pixels ($\widehat{\sigma}_\phi \leq 0.6$) for different threshold values of $\widehat{D}_A$, given our model distributions of noise standard deviation for data acquired over Volcán Alcedo.
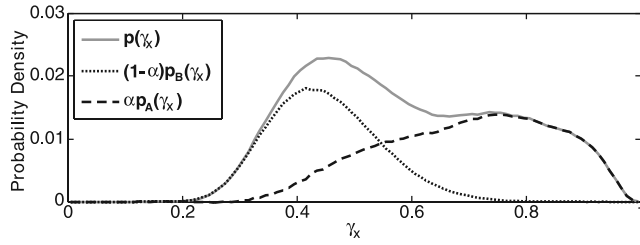
Figure C1. An example probability density for γ_x, shown in gray, for a given range of $\widehat{D}_{A,x}$. The probability density is the sum of two scaled probability densities, that for PS pixels, shown by the dashed line, and that for non-PS pixels, shown by the dotted line.

choosing pixels with $\widehat{D}_A < 0.25$ does not necessarily imply good phase stability.

[82] The phase analysis steps of PS methods that rely on a functional model of temporal deformation to identify PS pixels require an initial selection of pixels as PS candidates. These candidates should provide spatial coverage of at least 3 to 4 candidates/km^2 [*Colesanti et al.*, 2003b] and most of the candidates must be stable [*Kampes*, 2005]. Figure B4 shows, for the Alcedo data set, the percentage of area that meets the minimum candidate density requirement and the percentage of candidates that have good phase stability, for any chosen $\widehat{D}_A$ threshold. If using $\widehat{D}_A$ to pick the candidates, the density requirement pushes the $\widehat{D}_A$ threshold value up and the stability requirement pushes it down; hence there is no value that satisfies both requirements for the Alcedo data set.

[83] The phase analysis step in StaMPS does not require that most PS candidates are in fact PS pixels, so we are free to set $\widehat{D}_A$ as high as we like. Our criterion for phase stability is also more relaxed than $\widehat{\sigma}_\phi \leq 0.6$, as we expect PS pixels in rural areas to have lower SNR than those in urban areas. Our only requirement is that the signal be distinguishable from the noise, and on this basis we find PS pixels even in the Mount St. Helens data set. In theory, we could run the phase analysis step with no $\widehat{D}_A$ thresholding at all, but in practice computational times are greatly improved by thresholding. We choose a threshold value of $\widehat{D}_A$ that reduces the data volume by about an order of magnitude and includes most low simulated $\widehat{\sigma}_\phi$ values. This is typically in the region of 0.4.

Appendix C: PS Probability

[84] We expect a correlation between γ_x and the probability that pixel x is a PS pixel. By binning and normalizing the values of γ_x we can estimate the probability density of γ_x, $p(\gamma_x)$. We treat our population of pixels as the union of two populations, population A containing only PS pixels and population B containing only non-PS pixels; $p(\gamma_x)$ is, then, a weighted sum of the probability density for the PS pixels, $p_A(\gamma_x)$, and the probability density for the non-PS pixels, $p_B(\gamma_x)$ (see Figure C1), i.e.,

$$p(\gamma_x) = \alpha p_A(\gamma_x) + (1 - \alpha)p_B(\gamma_x), \tag{C1}$$

where $0 \leq \alpha \leq 1$. In order to derive $p_B(\gamma_x)$, we simulate 10^6 pseudopixels with random phase, i.e., $W\{\psi_{x,i} - \widetilde{\psi}_{x,i}\} =$

$\exp(\sqrt{-1}R)$, where R is a random variable in the interval $[-\pi, \pi]$, and follow the steps described above to arrive at a value of γ_x for each pseudopixel. We bin these values and normalize the distribution to obtain an estimate for $p_B(\gamma_x)$. For low values of γ_x, i.e., ≤ 0.3, $p_A(\gamma_x) \approx 0$ which implies

$$\int_0^{0.3} p(\gamma_x)\, d\gamma_x = (1 - \alpha) \int_0^{0.3} p_B(\gamma_x)\, d\gamma_x. \tag{C2}$$

[85] We use the data to evaluate the integral on the left-hand side and the simulation to evaluate the integral on the right-hand side. Thus we are able to estimate a conservative value for α. For pixel x, the probability that it is a PS pixel is

$$P(x \in A) = 1 - \frac{(1 - \alpha)p_B(\gamma_x)}{p(\gamma_x)}. \tag{C3}$$

[86] In practice, due to the presence of noise, the function $p_B(\gamma_x)/p(\gamma_x)$ may not be monotonically decreasing as expected, so we smooth it first by convolution with a 7 point Gaussian window.

References

Adam, N., B. Kampes, and M. Eineder (2005), Development of a scientific permanent scatterer system: Modifications for mixed ERS/ENVISAT time series, *Eur. Space Agency Spec. Publ., ESA SP-572*, 457–465.

Amelung, F., S. Jónsson, H. Zebker, and P. Segall (2000), Widespread uplift and 'trapdoor' faulting on Galapagos volcanoes observed with radar interferometry, *Nature, 407*(6807), 993–996.

Arnaud, A., J. Closa, R. Hanssen, N. Adam, M. Eineder, J. Inglada, G. Fitoussi, and B. Kampes (2004), Development of algorithms for the exploitation of ERS-Envisat using the stable points network, *Tech. Rep. ESA Contract 16702/02/I-LG*, Altamira Inf., Barcelona, Spain.

Arrigoni, M., C. Colesanti, A. Ferretti, D. Perissin, C. Prati, and F. Rocca (2004), Identification of the location phase screen of ERS-ENVISAT permanent scatterers, *Eur. Space Agency Spec. Publ., ESA SP-550*, 181–186.

Bamler, R. (2000), Interferometric stereo radargrammetry: Absolute height determination from ERS-ENVISAT interferograms, paper presented at International Geoscience and Remote Sensing Symposium, Geosci. and Remote Sens. Soc., Honolulu, Hawaii, 24–28 July.

Bamler, R., and D. Just (1993), Phase statistics and decorrelation in SAR interferograms, paper presented at International Geoscience and Remote Sensing Symposium, Geosci. and Remote Sens. Soc., Tokyo.

Chadwick, W. W., D. J. Geist, S. Jónsson, M. Poland, D. J. Johnson, and C. M. Meertens (2006), A volcano bursting at the seams: Inflation, faulting, and eruption at Sierra Negra Volcano, Galápagos, *Geology, 34*(12), 1025–1028.

Colesanti, C., A. Ferretti, F. Novali, C. Prati, and F. Rocca (2003a), SAR monitoring of progressive and seasonal ground deformation using the permanent scatterers technique, *IEEE Trans. Geosci. Remote Sens., 41*(7), 701–1685.

Colesanti, C., A. Ferretti, C. Prati, and F. Rocca (2003b), Monitoring landslides and tectonic motions with the permanent scatterers technique, *Eng. Geol, 68*(1–2), 3–14.

Crosetto, M., A. Arnaud, J. Duro, E. Biescas, and M. Agudo (2003), Deformation monitoring using remotely sensed radar interferometric data, paper presented at 11th International FIG Symposium on Deformation Measurements, Geod. and Geod. Appl. Lab., Dep. of Civ. Eng., Patras Univ., Santorini, Italy.

Efron, B., and R. Tibshirani (1986), Bootstrap methods for standard errors, confidence intervals, and other measures of statistical accuracy, *Stat. Sci.*, *1*(1), 54–77.

Ferretti, A., C. Prati, and F. Rocca (2000), Nonlinear subsidence rate estimation using permanent scatterers in differential SAR interferometry, *IEEE Trans. Geosci. Remote Sens.*, *38*(5), 2202–2212.

Ferretti, A., C. Prati, and F. Rocca (2001), Permanent scatterers in SAR interferometry, *IEEE Trans. Geosci. Remote Sens.*, *39*(1), 8–20.

Ferretti, A., F. Novali, R. Bürgmann, G. Hilley, and C. Prati (2004), InSAR permanent scatterer analysis reveals ups and downs in the San Francisco Bay Area, *Eos Trans. AGU*, *85*(34), 317–324.

Geist, D., K. A. Howard, A. M. Jellinek, and S. Rayder (1994), The volcanic history of volcan-alcedo, Galapagos Archipelago—A case-study of rhyolitic oceanic volcanism, *Bull. Volcanol.*, *56*(4), 243–260.

Goldstein, R. M., and C. L. Werner (1998), Radar interferogram filtering for geophysical applications, *Geophys. Res. Lett.*, *25*(21), 4035–4038.

Green, J. (1994), Recent activity in Alcedo volcano, Isabela island, *Not. Galápagos*, *54*, 11–13.

Hanssen, R. F. (2001), *Radar Interferometry Data Interpretation and Error Analysis*, 328 pp., Springer, New York.

Hilley, G. E., R. Burgmann, A. Ferretti, F. Novali, and F. Rocca (2004), Dynamics of slow-moving landslides from permanent scatterer analysis., *Science*, *304*(5679), 1952–1955.

Hole, J. K., A. Hooper, G. Wadge, and N. F. Stevens (2006), Measuring contemporary deformation in the Taupo volcanic zone, New Zealand, using SAR interferometry, in *Fringe 2005 Workshop, Proceedings of the Conference held 28 November–2 December, 2005 in Frascati, Italy* [CD-ROM], edited by H. Lacoste and L. Ouwehand, *Eur. Space Agency Spec. Publ., ESA-SP 610.*

Hooper, A., and H. Zebker (2007), Phase unwrapping in three dimensions with application to InSAR time series, *J. Opt. Soc. Am. A*, in press.

Hooper, A., H. Zebker, P. Segall, and B. Kampes (2004), A new method for measuring deformation on volcanoes and other natural terrains using InSAR persistent scatterers, *Geophys. Res. Lett.*, *31*, L23611, doi:10.1029/2004GL021737.

Johanson, I., and R. Bürgmann (2001), Using point measurements from InSAR to detect transient deformation, *Eos Trans. AGU*, *82*(47), Fall Meet. Suppl., Abstract G31A-0127.

Jónsson, S. (2002), Modeling volcano and earthquake deformation from satellite radar interferometric observations, Ph.D. thesis, Stanford Univ., Stanford, Calif.

Kampes, B. M. (2005), Displacement parameter estimation using permanent scatterer interferometry, Ph.D. thesis, Delft Univ. of Technol., Delft, Netherlands.

Kohlhase, A. O., K. L. Feigl, and D. Massonnet (2003), Applying differential InSAR to orbital dynamics: A new approach for estimating ERS trajectories, *J. Geod.*, *77*, 493–502, doi:10.1007/s00190-003-0336-3.

Lyons, S., and D. Sandwell (2003), Fault creep along the southern San Andreas from interferometric synthetic aperture radar, permanent scatterers, and stacking, *J. Geophys. Res.*, *108*(B1), 2047, doi:10.1029/2002JB001831.

Mosegaard, K., and A. Tarantola (1995), Monte Carlo sampling of solutions to inverse problems, *J. Geophys. Res.*, *100*(B7), 12,431–12,447.

Sigmundsson, F., H. Vadon, and D. Massonnet (1997), Readjustment of the Krafla spreading segment to crustal rifting measured by satellite radar interferometry, *Geophys. Res. Lett.*, *24*(15), 1843–1846.

Teunissen, P. J. G. (1995), The least-squares ambiguity decorrelation adjustment: A method for fast GPS integer ambiguity estimation, *J. Geod.*, *70*(1/2), 65–82.

Werner, C., U. Wegmüller, T. Strozzi, and A. Wiesmann (2003), Interferometric point target analysis for deformation mapping, paper presented at International Geoscience and Remote Sensing Symposium, Geosci. and Remote Sens. Soc., Toulouse, France.

Wessel, P., and W. H. F. Smith (1998), New, improved version of the generic mapping tools released, *Eos Trans. AGU*, *79*, 579.

Yang, X. M., P. M. Davis, and J. H. Dieterich (1988), Deformation from inflation of a dipping finite prolate spheroid in an elastic half-space as a model for volcanic stressing, *J. Geophys. Res.*, *93*(B5), 4249–4257.

Yun, S., P. Segall, and H. Zebker (2006), Constraints on magma chamber geometry at Sierra Negra Volcano, Galapagos islands, based on InSAR observations, *J. Volcanol. Geotherm. Res.*, *150*(1–3), 232–243.

Zebker, H. A., and J. Villasenor (1992), Decorrelation in interferometric radar echoes, *IEEE Trans. Geosci. Remote Sens.*, *30*(5), 950–959.

———————————

A. Hooper, Nordic Volcanological Center, Institute of Earth Sciences, Askja, Sturlugata 7, University of Iceland, Reykjavik, Iceland. (ahooper@hi.is)

P. Segall and H. Zebker, Department of Geophysics, Stanford University, Stanford, CA 94305, USA.